bioRxiv preprint doi: https://doi.org/10.1101/796581; this version posted October 10, 2019. The copyright holder for this preprint (which was not certified by peer review) is the author/funder, who has granted bioRxiv a license to display the preprint in perpetuity. It is made available under aCC-BY-NC 4.0 International license.

Human iPSC modeling elucidates mutation-specific responses to gene therapy in a genotypically diverse dominant maculopathy

Divya Sinha[1,2]*, Benjamin Steyer[1,3]*, Pawan K. Shahi[1,4], Katherine Mueller[3], Rasa Valiauga[2], Kimberly L. Edwards[2], Cole Bacig[2], Stephanie S. Steltzer[3], Sandhya Srinivasan[3], Amr Abdeen[3], Evan Cory[3], Viswesh Periyasamy[3], Alireza Fotuhi Siahpirani[3], Sushmita Roy[3,5], Bikash R. Pattnaik[1,4,6]**, Krishanu Saha[1,3,7]**, David M. Gamm[1,2,6]**^

[1]McPherson Eye Research Institute, University of Wisconsin-Madison, Madison, WI, USA

[2]Waisman Center, University of Wisconsin-Madison, Madison, WI, USA

[3]Wisconsin Institute for Discovery, University of Wisconsin-Madison, Madison, WI, USA

[4]Department of Pediatrics, University of Wisconsin-Madison, Madison, WI, USA

[5]Department of Biostatistics, University of Wisconsin-Madison, Madison, WI, USA

[6] Department of Ophthalmology and Visual Sciences, University of Wisconsin-Madison, Madison, WI, USA

[7]Department of Biomedical Engineering, University of Wisconsin-Madison, Madison, WI, USA

* These authors contributed equally to the work

Co-Correspondence: D.M.G. (dgamm@wisc.edu), K.S. (ksaha@wisc.edu), and B. R. P. (pattnaik@wisc.edu)

^ **Lead contact:** D.M.G.

Subject Terms: human pluripotent stem cells, gene therapy, somatic cell genome editing CRISPR-Cas9, gene augmentation, autosomal dominant disease, macular degeneration, orphan disease, channelopathy

bioRxiv preprint doi: https://doi.org/10.1101/796581; this version posted October 10, 2019. The copyright holder for this preprint (which was not certified by peer review) is the author/funder, who has granted bioRxiv a license to display the preprint in perpetuity. It is made available under aCC-BY-NC 4.0 International license.

SUMMARY

Dominantly inherited disorders are not typically considered therapeutic candidates for gene augmentation (GA). We tested whether GA or genome editing (GE) could serve as a solo therapy for autosomal dominant Best disease (adBD), a macular dystrophy linked to over 100 mutations in the *BEST1* gene, which encodes a homo-pentameric calcium-activated chloride channel (CaCC) in the retinal pigment epithelium (RPE). Since no suitable animal models of adBD exist, we generated RPE from patient-derived induced pluripotent stem cells (iPSC-RPE) and found that GA restored CaCC activity and improved rhodopsin degradation in a subset of adBD lines. iPSC-RPE harboring adBD mutations in calcium clasp or chloride binding domains of the channel, but not in a putative structural region, were responsive to GA. However, reversal of the iPSC-RPE CaCC deficit was demonstrated in every adBD line following targeted CRISPR-Cas9 GE of the mutant allele. Importantly, 95% of GE events resulted in premature stop codons within the mutant allele, and single cell profiling demonstrated no adverse perturbation of RPE transcriptional programs post-editing. These results show that GA is a viable approach for a subset of adBD patients depending on the functional role of the mutated residue. Further, GA non-responders are candidates for targeted GE of the mutant allele. Similar scenarios likely exist for other genotypically diverse dominant diseases, expanding the therapeutic landscape for affected patients.

INTRODUCTION

Genotypically heterogeneous dominant diseases pose significant challenges and opportunities for precision medicine (Doudna and Charpentier, 2014). Among gene therapies, GA for recessive disorders is the most developed, having spurred multiple clinical trials (Cukras et al., 2018; Lam et al., 2019; Russell et al., 2017) and FDA approval for one ocular disease (Ledford, 2017). However, GA is generally ruled out as a stand-alone therapy for dominant disorders due to a perceived need to eliminate the deleterious

bioRxiv preprint doi: https://doi.org/10.1101/796581; this version posted October 10, 2019. The copyright holder for this preprint (which was not certified by peer review) is the author/funder, who has granted bioRxiv a license to display the preprint in perpetuity. It is made available under aCC-BY-NC 4.0 International license.

effects of the mutant (MT) allele. While GE holds promise in this regard (Bakondi et al., 2016; Li, 2018; Tsai et al., 2018), testing safety and efficacy for every GE target mutation using MT allele-targeted single guide RNAs (sgRNAs) presents practical and economic barriers. Further, GE cannot correct all mutations (Bakondi et al., 2016; Courtney et al., 2016; Pattanayak et al., 2013) and may lead to off-target mutagenesis—particularly within the heterozygous wildtype (WT) allele in dominant diseases—or other adverse events (Cromer et al., 2018). As such, it is prudent to maximize use of GA in cases where it is deemed safe and efficacious and reserve GE strategies for those patients who truly require it.

Best disease, a common type of inherited macular degeneration, is a genotypically complex disorder transmitted predominantly as adBD, although rare cases of autosomal recessive bestrophinopathy (ARB) are known (Johnson et al., 2017). Both adBD and ARB are caused by missense mutations in the *BEST1* gene, which is expressed in the RPE, a monolayer of cells essential for the survival and function of photoreceptors. While canine models of ARB closely mimic the human phenotype (Guziewicz et al., 2017), no animal models of adBD exist. To provide a therapeutic testing platform for adBD, we previously developed the first human iPSC-RPE models of the disease, which demonstrated relevant cellular dysfunction; most notably, delayed degradation of phagocytosed photoreceptor outer segment (POS) proteins (Singh et al., 2015; Singh et al., 2013b). Recently, the high-resolution crystal structure of WT BEST1 was elucidated, which revealed it to be a homo-pentameric CaCC (Dickson et al., 2014; Yang et al., 2014) (**Figure 1A**). Mutation hotspots in BEST1 were found to lie within calcium or chloride ion binding sites, or contribute to the structural organization of the channel, among other roles (Dickson et al., 2014). Our two prior adBD iPSC-RPE models harbored mutations in a calcium binding (N296H) or structural (A146K) domain (Singh et al., 2015; Singh et al., 2013b). Therefore, for the present study, we generated iPSCs from a third patient with adBD caused by a chloride binding site mutation (R218C), as well as an ARB patient with compound heterozygous mutations (R141H/A195V) (**Figure 1B,C**). We also

bioRxiv preprint doi: https://doi.org/10.1101/796581; this version posted October 10, 2019. The copyright holder for this preprint (which was not certified by peer review) is the author/funder, who has granted bioRxiv a license to display the preprint in perpetuity. It is made available under aCC-BY-NC 4.0 International license.

71 employed two control lines: a WT iPSC line and an isogenic line generated via CRISPR-based gene
72 correction of R218C adBD iPSCs (Steyer et al., 2018).
73
74 **RESULTS**
75 **BEST1 protein is robustly expressed in WT and adBD iPSC-RPE, but not ARB iPSC-RPE.**
76 The six iPSC lines were tested for pluripotency, differentiated to RPE, and characterized (**Data**
77 **S1**; **Figure S1; Table S1**). iPSC-RPE monolayers from all adBD and control lines, but not the ARB line,
78 showed robust expression of BEST1 protein (**Figure S1D**). The profoundly decreased BEST1 expression
79 in our ARB cultures is consistent with reports using heterologous expression systems that showed low or
80 undetectable levels of R141H or A195V BEST1 (Milenkovic et al., 2018).
81
82 **Virus-mediated *BEST1* GA restores CaCC activity and enhances POS degradation in ARB iPSC-**
83 **RPE.**
84 We next sought to confirm that ectopic expression of wildtype human BEST1 (hBEST1) could
85 ameliorate the disease phenotype of R141H/A195V ARB iPSC-RPE, analogous to GA studies using ARB
86 canines or other iPSC-RPE model systems for ARB (Guziewicz et al., 2018; Li et al., 2017). For readouts
87 of efficacy, we performed single-cell patch clamp recordings of calcium-activated chloride current
88 density—a measurement of CaCC activity—which was greatly reduced in ARB iPSC-RPE cells relative
89 to WT iPSC-RPE (**Figure 1D; Figure S2**). As an assay of intact RPE monolayer function, we also
90 monitored degradation of rhodopsin following POS feeding (**Figure 2**).
91 For GA we used a lentivirus (LV) construct (*hVMD2-hBEST1-T2A-GFP*) (**Figure 2A**) designed to
92 co-express hBEST1 and GFP under control of the human *BEST1* promoter (*hVMD2*) in order to restrict
93 hBEST1 expression to RPE. Although adeno-associated virus (AAV) is commonly employed for gene

bioRxiv preprint doi: https://doi.org/10.1101/796581; this version posted October 10, 2019. The copyright holder for this preprint (which was not certified by peer review) is the author/funder, who has granted bioRxiv a license to display the preprint in perpetuity. It is made available under aCC-BY-NC 4.0 International license.

delivery *in vivo*, LV has also been used in human retinal gene therapy trials (Waugh et al., 2018) (ClinicalTrials.gov Identifiers: NCT01367444, NCT01736592) and efficiently transduces cultured human RPE (Pawan K. Shahi, 2019; Singh et al., 2013b). GFP expression was observed in ARB iPSC-RPE cells starting one-week post-transduction (**Figure S3A**) and immunocytochemical (ICC) analysis confirmed enhanced expression of BEST1 (**Figure S3B**). By ≥4 weeks post-LV transduction, CaCC current density in ARB iPSC-RPE increased significantly, reaching levels comparable to WT iPSC-RPE (**Figure 2D,I,J; Extended Figure 3C**). Furthermore, transduced monolayers of ARB iPSC-RPE demonstrated enhanced degradation of rhodopsin following POS feeding (**Figure 2E**). These findings, together with those reported by Guziewicz et al. (Guziewicz et al., 2018) and Li et al. (Li et al., 2017), support virus-mediated *hBEST1* GA as a treatment for ARB.

BEST1 GA also restores CaCC activity and enhances POS degradation in iPSC-RPE derived from some—but not all—adBD lines.

Although not as intuitive, we also suspected that GA might be a viable solo therapeutic strategy for a subset of adBD-causing mutations. Based on the eukaryotic BEST1 crystal structure, we hypothesized that mutations affecting chloride or calcium ion binding sites would not affect gross structure of the channel, but rather reduce its regulatory response and/or ion conductance capacity proportional to the ratio of WT versus MT monomers. If so, we would expect increased CaCC activity simply by shifting this ratio toward incorporation of more WT monomers through GA (**Figure 2F**).

Similar to ARB iPSC-RPE, CaCC activity in iPSC-RPE from all three adBD lines was diminished compared to control (**Figure 2G (*left*); Figure S2C,E,F**). Single-cell patch clamp experiments on the gene-corrected R218C>WT isogenic iPSC-RPE control showed CaCC current density at levels similar to native WT control lines (**Figure S2D**), confirming that the diminished CaCC activity is indeed the result

bioRxiv preprint doi: https://doi.org/10.1101/796581; this version posted October 10, 2019. The copyright holder for this preprint (which was not certified by peer review) is the author/funder, who has granted bioRxiv a license to display the preprint in perpetuity. It is made available under aCC-BY-NC 4.0 International license.

of the mutation. The *hVMD2-hBEST1-T2A-GFP* LV construct was then used to transduce iPSC-RPE from all three adBD patients (**Figure S3D**). At ≥4 weeks post-transduction, CaCC activity was restored in iPSC-RPE containing mutations in a chloride (R218C) or calcium (N296H) binding site, whereas iPSC-RPE harboring the A146K mutation, which resides in a structural domain of the channel, did not show restoration of CaCC activity (**Figure 2G,I,J; Figure S3E-G**). Consistent with these single-cell electrophysiological findings, GA improved rhodopsin degradation in R218C and N296H iPSC-RPE, but not in A146K iPSC-RPE (**Figure 2H**).

GE specifically disrupts the MT allele in adBD iPSCs and iPSC-RPE with high efficiency and negligible off-target editing.

To determine whether A146K iPSC-RPE would respond to an alternative therapeutic approach, we tested GE as a means to eliminate expression of the MT *BEST1* allele (**Figure 3A**). GE with CRISPR-Cas9 creates targeted double strand breaks in genomic DNA that are primarily repaired by endogenous non-homologous end joining (NHEJ) (Cox et al., 2015), leading to insertion and deletion mutations (indels). These indels can cause transcriptional frameshifts that lead to premature termination codons, activation of intrinsic nonsense-mediated decay (NMD) pathways, and degradation of transcription products (Popp and Maquat, 2016). Since we previously demonstrated successful targeting of the R218C MT allele using sgRNAs (Steyer et al., 2018), sequences targeting the R218 locus in either the MT or the WT allele were cloned into a LV plasmid that encoded both the sgRNA and a human codon optimized *Streptococcus pyogenes Cas9* (*spCas9)-T2A-reporter* transcript (**Figure 3B,C**).

Using these GE constructs, we first transduced both undifferentiated R218C adBD iPSCs and gene-corrected, isogenic control, R218C>WT iPSCs. In R218C>WT iPSCs, we observed a dose-dependent increase in percent edited alleles after GE treatment with LV encoding WT sgRNA, but no

bioRxiv preprint doi: https://doi.org/10.1101/796581; this version posted October 10, 2019. The copyright holder for this preprint (which was not certified by peer review) is the author/funder, who has granted bioRxiv a license to display the preprint in perpetuity. It is made available under aCC-BY-NC 4.0 International license.

editing after treating with LV encoding MT (R218C) targeted sgRNA (**Figure 3D *left***). However, in R218C iPSCs we observed editing after GE with both WT sgRNA and R218C sgRNA (**Figure 3D *right***). Similarly, GE of iPSC-RPE with R218C sgRNA revealed a dose dependent increase in editing in R218C iPSC-RPE with minimal editing in R218C>WT iPSC-RPE (**Figure 3E**). Together, these results indicate high specificity of the R218C sgRNA for the MT allele over the heterozygous WT allele. Observation of minimal editing (1.6% max, ratio of MT:WT editing = 19.5; **Supplemental Data File A**) at the non-targeted WT allele in iPSC-RPE, but not in undifferentiated iPSCs, may reflect open chromatin around the actively transcribed *BEST1* locus in iPSC-RPE (Kuscu et al., 2014). Notably, an average of 95% of the edited alleles in iPSC-RPE resulted in a frameshift mutation (**Figure 3F,G *bottom*; Supplemental Data File A**), which is higher than the 70% frameshift rate observed in iPSCs (**Figure 3F,G *top***) or predicted using a recent machine learning algorithm (Shen et al., 2018) (**Supplemental Data File B**).

Next, we performed an off-target analysis after GE of R218C iPSCs (**Figure S4**) or R218C iPSC-RPE (**Figure 3H**) with the R218C sgRNA. Analysis of the top nine off-target sites revealed measurable off-target editing only at the second-ranked locus, which maps to an unannotated region on chromosome 7, 140 kb from any known transcription product. Conversely, we observed overall editing of 24.9% ± 4.5% [SD] at the on-target (*BEST1*) locus in iPSC-RPE (**Figure 3H**). Due to high specificity of the R218C sgRNA for the R218C allele, this equates to editing in approximately 50% of the MT alleles.

To evaluate for NMD, we quantified WT and MT (R218C + edited) sequencing reads from both DNA and RNA isolated from iPSC-RPE cultures after GE (**Figure S5**). We observed a significant increase in the ratio of WT to MT RNA in GE versus control groups; however, no such increase was observed in the ratio of WT to MT DNA allele frequency between these groups (**Figure 3I**). Together, these data indicate significant degradation of MT transcripts following GE, presumably through NMD.

bioRxiv preprint doi: https://doi.org/10.1101/796581; this version posted October 10, 2019. The copyright holder for this preprint (which was not certified by peer review) is the author/funder, who has granted bioRxiv a license to display the preprint in perpetuity. It is made available under aCC-BY-NC 4.0 International license.

MT allele-specific GE restores CaCC activity in iPSC-RPE derived from all tested adBD lines with no demonstrable change in the RPE transcriptional signature.

We next assessed phenotypic rescue in control versus GE iPSC-RPE using LV vectors expressing sgRNAs targeting specific alleles. Single-cell patch clamp experiments revealed restoration of CaCC activity in R218C, N296H, and A146K iPSC-RPE cells (**Figure 3J-L; Figure S6**). Finally, to search for off-target or other untoward transcriptional effects from GE, we performed single-cell RNA sequencing (scRNA-seq) for 12,061 individual iPSC-RPE cells treated with GE. iPSC-RPE (R218C, N296H, A146K, or gene-corrected R218C>WT) were edited with vectors encoding *spCas9-T2A-GFP* and either a MT allele-targeted sgRNA or a control sgRNA targeting the *AAVS1* safe harbor locus (Sadelain et al., 2011), to generate a total of eight separate samples (**Figure S7**).

Evaluation of t-Distributed Stochastic Neighbor Embedding (t-SNE) clustering of cells across all eight samples indicated that, by virtue of using the *hVMD2* promoter, *spCas9-T2A-GFP* transcript levels closely correspond with *BEST1* transcript levels (**Figure 3M**). Visual comparison of t-SNE clustering of each individual sample demonstrated that transcriptional signatures are grossly similar between iPSC-RPE lines whether treated with MT allele-targeted (+GE) or control (*AAVS1*) sgRNA (**Figure 3N *top***). This observation was supported quantitatively by non-negative matrix factorization (NMF). NMF analysis demonstrated that greater transcriptome variation exists between iPSC-RPE from different lines than between iPSC-RPE from the same line treated with MT allele-targeted or control sgRNA (**Figure S7B**).

Additional analysis of global gene expression (**Figure 3N *bottom***) and of a focused set of genes related to negative or off-target effects (including cell cycle regulation, apoptosis, DNA damage response, or innate immune response; **Figure S7C**) did not reveal significant upregulation of those gene sets in MT allele-targeted (+GE) versus control sgRNA-treated samples.

bioRxiv preprint doi: https://doi.org/10.1101/796581; this version posted October 10, 2019. The copyright holder for this preprint (which was not certified by peer review) is the author/funder, who has granted bioRxiv a license to display the preprint in perpetuity. It is made available under aCC-BY-NC 4.0 International license.

DISCUSSION

The observation that adBD mutations associated with ion binding may be amenable to GA greatly expands the patient population that might benefit from this therapeutic approach. However, the stark difference in functional response to GA among our adBD iPSC-RPE models underscores the need to vet patients for GA candidacy carefully. The mechanism underlying selective GA responsivity in adBD is not due to traditional allelic haploinsufficiency, in which half the normal amount of WT protein and no MT protein is produced, resulting in fewer (but fully WT) BEST1 channels. Such a situation exists in parents of ARB patients, who have no demonstrable disease phenotype. Rather, adBD MT monomers are incorporated alongside WT monomers in all (or nearly all) BEST1 channels, resulting in ion binding site insufficiency and channel impermeability, which is surmountable by WT *BEST1* GA. In contrast, we hypothesize that *BEST1* mutations like A146K—which converts a nonpolar amino acid to a polar amino acid in a structural region of the protein—has more pervasive functional consequences, resulting in resistance to GA even at low MT:WT monomer ratios. Whether such mutations eventually can be overcome by GA via increasing the expression levels of the WT transgene is yet to be determined.

There is precedence for using patient-specific iPSCs as preclinical efficacy models for gene therapy (Vasireddy et al., 2013). Our work extends this capability by providing a framework for preclinical testing of mutation-specific responses in a genotypically heterogenous disease. It remains to be determined whether separate adBD iPSC-RPE models will be required to assess suitability of GA versus GE for every mutation, or if a few models can sufficiently represent larger categories of mutations (*e.g.*, ion binding sites or structural regions).

For adBD mutations like A146K that are not amenable to GA, we showed that targeted GE holds promise as a future therapy. Importantly, we observed high efficiency out-of-frame editing in iPSC-RPE compared to undifferentiated iPSCs. This result is consistent with recent reports of variable mutation bias

bioRxiv preprint doi: https://doi.org/10.1101/796581; this version posted October 10, 2019. The copyright holder for this preprint (which was not certified by peer review) is the author/funder, who has granted bioRxiv a license to display the preprint in perpetuity. It is made available under aCC-BY-NC 4.0 International license.

209 across different cell types (Shen et al., 2018), and points to the importance of evaluating GE using specific
210 cell type(s) targeted by disease, and not surrogate cell types. In addition, editing at *BEST1* in iPSC-RPE
211 did not provoke an increase in expression of genes associated with cell cycle regulation, apoptosis, DNA
212 damage response, or innate immune response in comparison to editing at a well characterized safe-harbor
213 locus (Sadelain et al., 2011) with a previously described sgRNA (Mali et al., 2013). This is in contrast to
214 studies in other cell types that have reported potential for Cas9-mediated GE to provoke undesirable
215 effects, including innate immune response (Wienert et al., 2018) and apoptosis, among other concerns
216 (Cromer et al., 2018).

217 Our results provide a blueprint to guide gene therapy choice in the era of GA and GE. With its
218 inherently larger target populations and established track record in patients, it is practical to utilize GA
219 when possible, reserving GE for mutations that require allele repair or knockout or are otherwise
220 untreatable by GA. It is noteworthy that the two adBD lines that demonstrated restoration of CaCC
221 activity with GA or GE did so with equal efficacy, underscoring the suitability of Best disease for either
222 approach. Other desirable characteristics of Best disease as a clinical candidate for GA or GE include 1) a
223 wide time window for gene therapy intervention, 2) accessibility of RPE using standard surgical
224 techniques, 3) a small (5.5 mm diameter) treatment area, 4) availability of noninvasive retinal imaging
225 and functional assessment tools, and 5) growing patient safety data from other RPE-based gene therapy
226 trials (Cukras et al., 2018; Lam et al., 2019; Russell et al., 2017). As such, Best disease is well-positioned
227 to become the first genotypically heterogeneous disorder with dominant and recessive inheritance patterns
228 to have a full menu of therapeutics for all affected individuals. Furthermore, implications of this work
229 likely extend beyond the eye and Best disease to other intractable monogenic conditions caused by
230 mutations in multimeric ion channels, including congenital myasthenic syndromes and some forms of
231 epilepsy (George, 2004; Schaaf, 2014; Villa and Combi, 2016).

bioRxiv preprint doi: https://doi.org/10.1101/796581; this version posted October 10, 2019. The copyright holder for this preprint (which was not certified by peer review) is the author/funder, who has granted bioRxiv a license to display the preprint in perpetuity. It is made available under aCC-BY-NC 4.0 International license.

ACKNOWLEDGEMENTS

The authors thank Alfred Lewin (U. Florida) for the *hVMD2-hBEST1-T2A-GFP* plasmid construct; the Cellular Imaging and Analysis core at the University of Wisconsin-Madison Waisman Center; Budd Tucker and Ed Stone (U. Iowa) for providing the ARB iPSC line, corresponding Scorecard data, and ARB patient fundus images; and Andrew Thliveris for helpful discussions. This work was supported by NIH R01EY024588, Foundation Fighting Blindness, Research to Prevent Blindness, Retina Research Foundation Emmett Humble Chair, and McPherson Eye Research Institute Sandra Lemke Trout Chair in Eye Research (to D.M.G.); NSF CBET-1350178 and CBET-1645123, NIH R35GM119644, John Merck Fund Translational Research Program, Brain & Behavior Research Foundation, Burroughs Wellcome Fund (to K.S.); NIH R01EY024995 and Retina Research Foundation M.D. Mathews Professorship (to B.R.P.); NIH T32HG002760 and F30EY027699, VitreoRetinal Surgery Foundation (to B.S.); DGE-1747503 (to K.M.). This study was supported in part by a core grant to the Waisman Center (NICHHD U54 HD090256). We thank members of the Gamm and Saha labs for comments on the manuscript, plasmid depositors to Addgene, the University of Wisconsin-Madison Biotechnology Center for DNA sequencing, and the University of Wisconsin-Madison Skin Disease Research Center for assistance with virus preparation.

AUTHOR CONTRIBUTIONS

D.S. and D.M.G. designed the GA experiments. B.S., D.S., D.M.G. and K.S. designed the GE experiments. P.K.S. and B.R.P. performed and analyzed the electrophysiology experiments. D.S. and B.S. performed all other experiments with contributions from R.V., K.L.E., C.B, S.S.S., A.A., and E.C. K.M., S.S., V.P., A.F.S., and S.R. were primarily responsible for the scRNA-seq analysis. D.S., B.S., K.S., and

bioRxiv preprint doi: https://doi.org/10.1101/796581; this version posted October 10, 2019. The copyright holder for this preprint (which was not certified by peer review) is the author/funder, who has granted bioRxiv a license to display the preprint in perpetuity. It is made available under aCC-BY-NC 4.0 International license.

D.M.G. wrote the manuscript and analyzed data with input from all authors. D.M.G., K.S., and B.R.P. supervised research.

COMPETING INTERESTS STATEMENT

The authors declare no competing interests.

bioRxiv preprint doi: https://doi.org/10.1101/796581; this version posted October 10, 2019. The copyright holder for this preprint (which was not certified by peer review) is the author/funder, who has granted bioRxiv a license to display the preprint in perpetuity. It is made available under aCC-BY-NC 4.0 International license.

FIGURES AND FIGURE LEGENDS

Figure 1

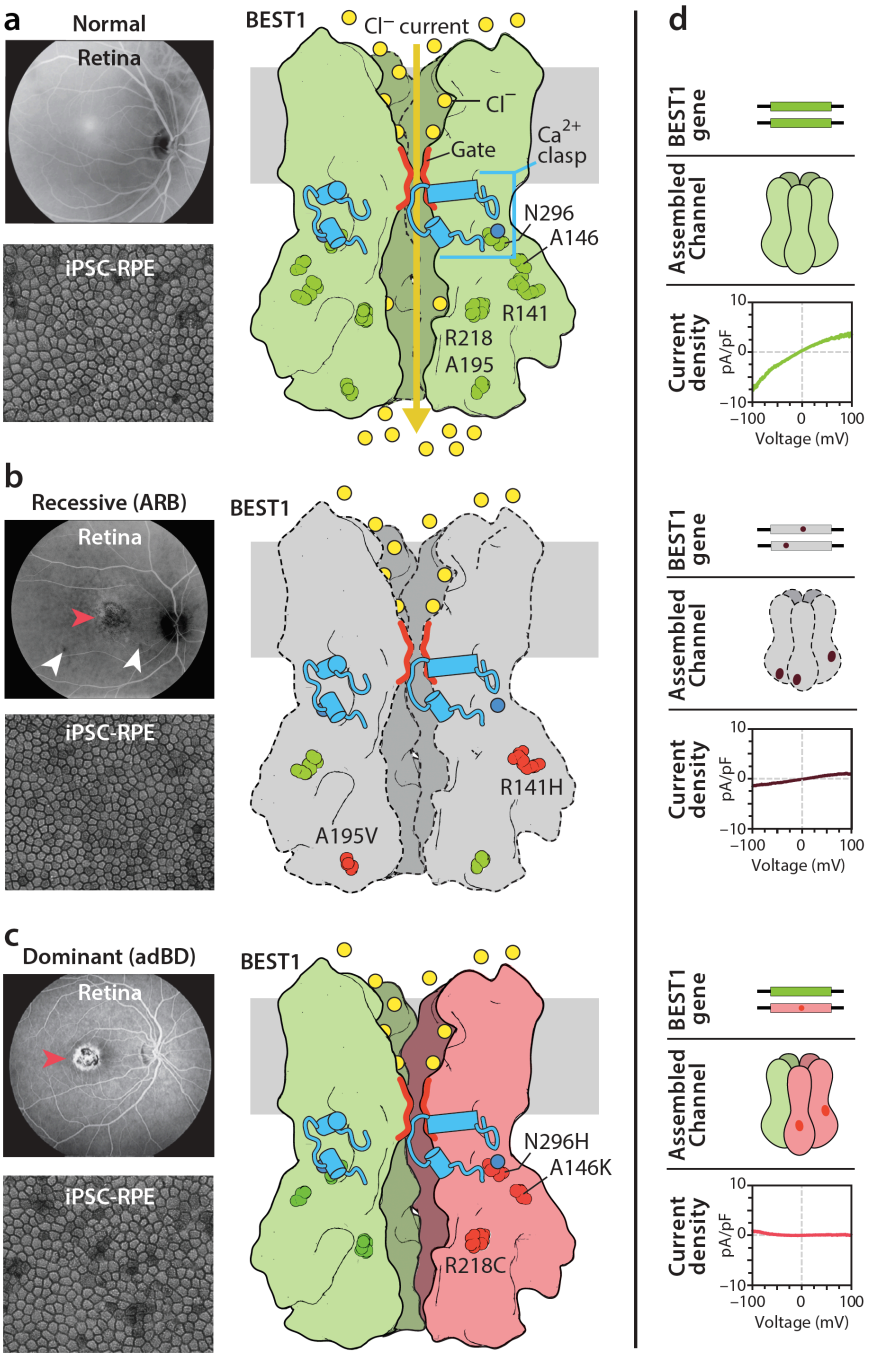

bioRxiv preprint doi: https://doi.org/10.1101/796581; this version posted October 10, 2019. The copyright holder for this preprint (which was not certified by peer review) is the author/funder, who has granted bioRxiv a license to display the preprint in perpetuity. It is made available under aCC-BY-NC 4.0 International license.

Figure 1 | *BEST1* mutations reduce CaCC current in Best disease iPSC-RPE. (A) Images (in grayscale) of a normal fundus (*top*) and control (WT) iPSC-RPE (*bottom*). A fully functional homo-pentameric BEST1 channel is formed by expression and assembly of WT alleles and subunits (*green*), respectively, allowing movement of chloride ions (*yellow* circles) upon binding of calcium ions (*blue* circle) (based on eukaryotic BEST1 crystal structure by Dickson et al. (Dickson et al., 2014)). **(B)** *Top*, Fundus image of an ARB patient with R141H/A195V compound heterozygous mutations in *BEST1* showing a vitelliform lesion in the macula (*red* arrowhead) as well as small lesions outside the macula (*white* arrowheads), which is characteristic of ARB. *Bottom*, iPSC-RPE derived from the same ARB patient. Pentameric channel assembly for these mutations is expected to be significantly reduced due to protein degradation (denoted by *gray* subunits with dashed outlines). **(C)** *Top,* Fundus image showing a vitelliform macular lesion (*red* arrowhead) in an adBD patient with a heterozygous R218C mutation in *BEST1*. *Bottom*, iPSC-RPE derived from the same adBD patient. Both adBD mutant (MT) (*red*) and WT (*green*) monomers are assembled in the pentameric channel. **(D)** CaCC current density-voltage plots from WT (*top*), R141H/A195V ARB (*middle*), or R218C adBD (*bottom*) iPSC-RPE cells, as determined by calculating the difference in average chloride currents in the presence or absence of calcium (**Figure S2**). For +calcium: n = 6 cells for WT, 12 cells for R141H/A195V ARB, and 5 cells for R218C adBD; for no calcium: n = 8 cells for WT, 12 cells for R141H/A195V ARB, and 8 cells for R218C adBD (data combined from at least two replicates). The number of cells from each replicate is listed in **Table S8**. See also Figures S1-S3.

bioRxiv preprint doi: https://doi.org/10.1101/796581; this version posted October 10, 2019. The copyright holder for this preprint (which was not certified by peer review) is the author/funder, who has granted bioRxiv a license to display the preprint in perpetuity. It is made available under aCC-BY-NC 4.0 International license.

Figure 2

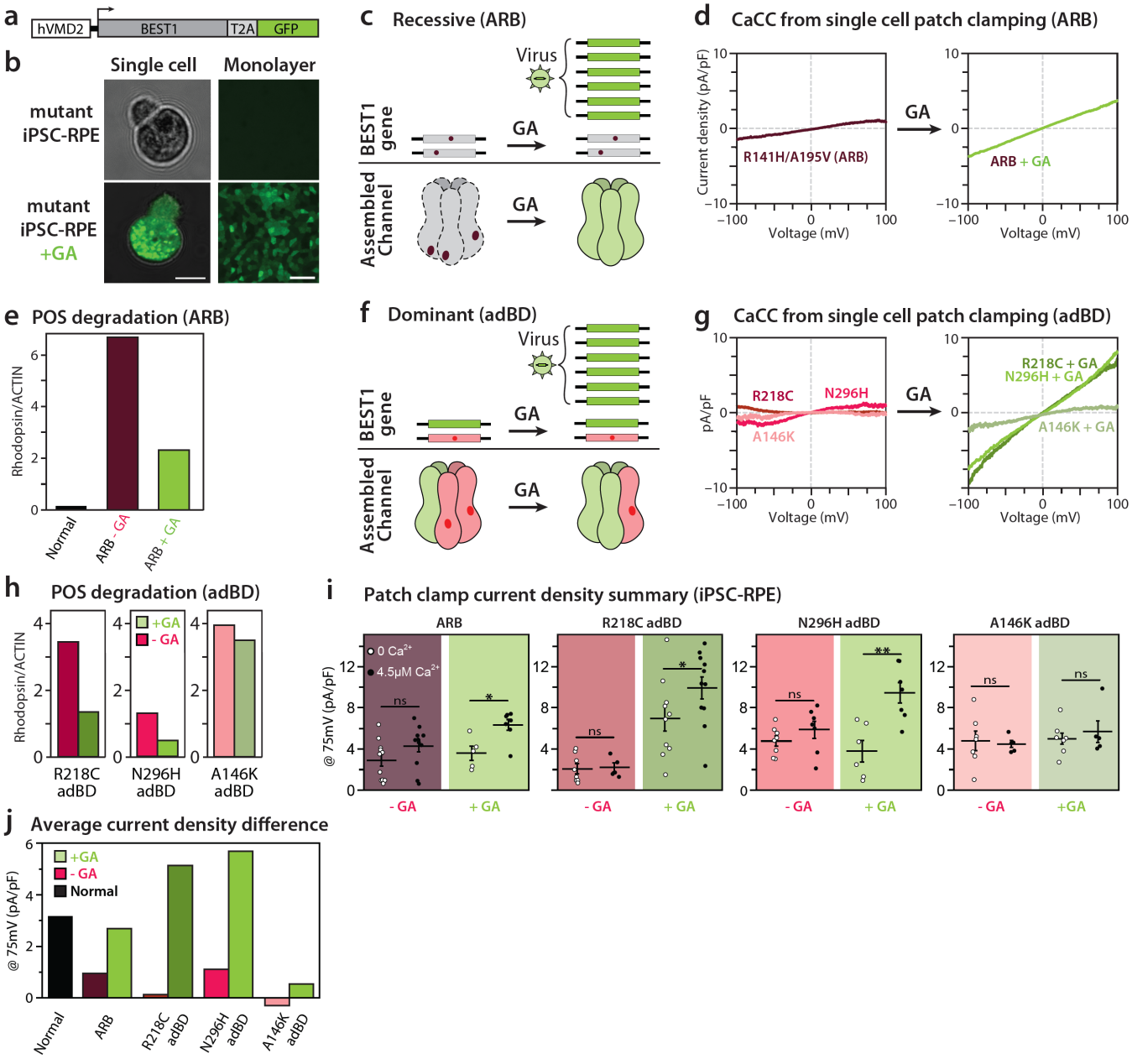

bioRxiv preprint doi: https://doi.org/10.1101/796581; this version posted October 10, 2019. The copyright holder for this preprint (which was not certified by peer review) is the author/funder, who has granted bioRxiv a license to display the preprint in perpetuity. It is made available under aCC-BY-NC 4.0 International license.

Figure 2 | Mutation-dependent rescue of Best disease phenotypes by gene augmentation (GA). (A) Construct used for BEST1 GA. **(B)** Presence or absence of GFP fluorescence in dissociated iPSC-RPE cells (*left*) or iPSC-RPE monolayers (*right*) before (*top*) or after (*bottom*) GA. Scale bar = 10 µm (*left*); 50 µm (*right*). **(C)** Rationale for GA in ARB: LV-mediated expression of WT hBEST1 (*green* subunits) will compensate for the lack of endogenous BEST1 expression (*gray* subunits) and increase formation of fully functional homo-pentameric BEST1 channels. **(D)** CaCC current density-voltage plots before (*left*) and after (*right*) GA of ARB iPSC-RPE. CaCC current density-voltage plot of ARB (-GA) is the same as shown in Figure 1d, and is included for comparison. For the ARB+GA condition, n = 7 cells for +calcium and 5 cells for no calcium (data combined from two replicates). The number of cells from each replicate is listed in **Table S8**. **(E)** Rhodopsin levels 120 hr after POS feeding in WT, ARB, and ARB+GA iPSC-RPE. The Western blot used for quantifying rhodopsin levels is shown in **Figure 2**. **(F)** Rationale for using GA in adBD: LV-meditated expression of WT hBEST1 (*green* subunits) will increase the ratio of WT:MT (*green*:*red* subunits) BEST1 monomers, thus improving channel function. **(G)** CaCC current density-voltage plots before (*left*) or after (*right*) GA of adBD iPSC-RPE. Before GA (*left* panel): for +calcium: n = 7 cells for N296H and 5 cells for A146K adBD; for no calcium: n = 8 cells for N296H and 7 cells for A146K (data combined from two replicates). The CaCC current density-voltage plot for R218C adBD (-GA) is the same as shown in Figure 1d, and is included for comparison. After GA (*right* panel): for +calcium: n = 11 cells for R218C, 7 cells for N296H, and 5 cells for A146K; for no calcium: n = 9 cells for R218C, 6 cells for N296H, and 8 cells for A146K (data combined from two replicates). The number of cells from each replicate is listed in **Table S8**. **(H)** Rhodopsin levels 48 hours after feeding POS to adBD iPSC-RPE with or without GA. Western blots used for quantifying rhodopsin levels are shown in **Data S2**. **(I)** CaCC conductance for individual iPSC-RPE cells, and **(J)** mean CaCC

bioRxiv preprint doi: https://doi.org/10.1101/796581; this version posted October 10, 2019. The copyright holder for this preprint (which was not certified by peer review) is the author/funder, who has granted bioRxiv a license to display the preprint in perpetuity. It is made available under aCC-BY-NC 4.0 International license.

conductance at 75 mV before or after GA. The number of cells is the same as for panels d and g. Error bars in 2i represent mean ± SEM; ns = $p \geq 0.05$, * for $p < 0.05$, ** for $p < 0.01$. See also Figures S1-S3.

bioRxiv preprint doi: https://doi.org/10.1101/796581; this version posted October 10, 2019. The copyright holder for this preprint (which was not certified by peer review) is the author/funder, who has granted bioRxiv a license to display the preprint in perpetuity. It is made available under aCC-BY-NC 4.0 International license.

Figure 3

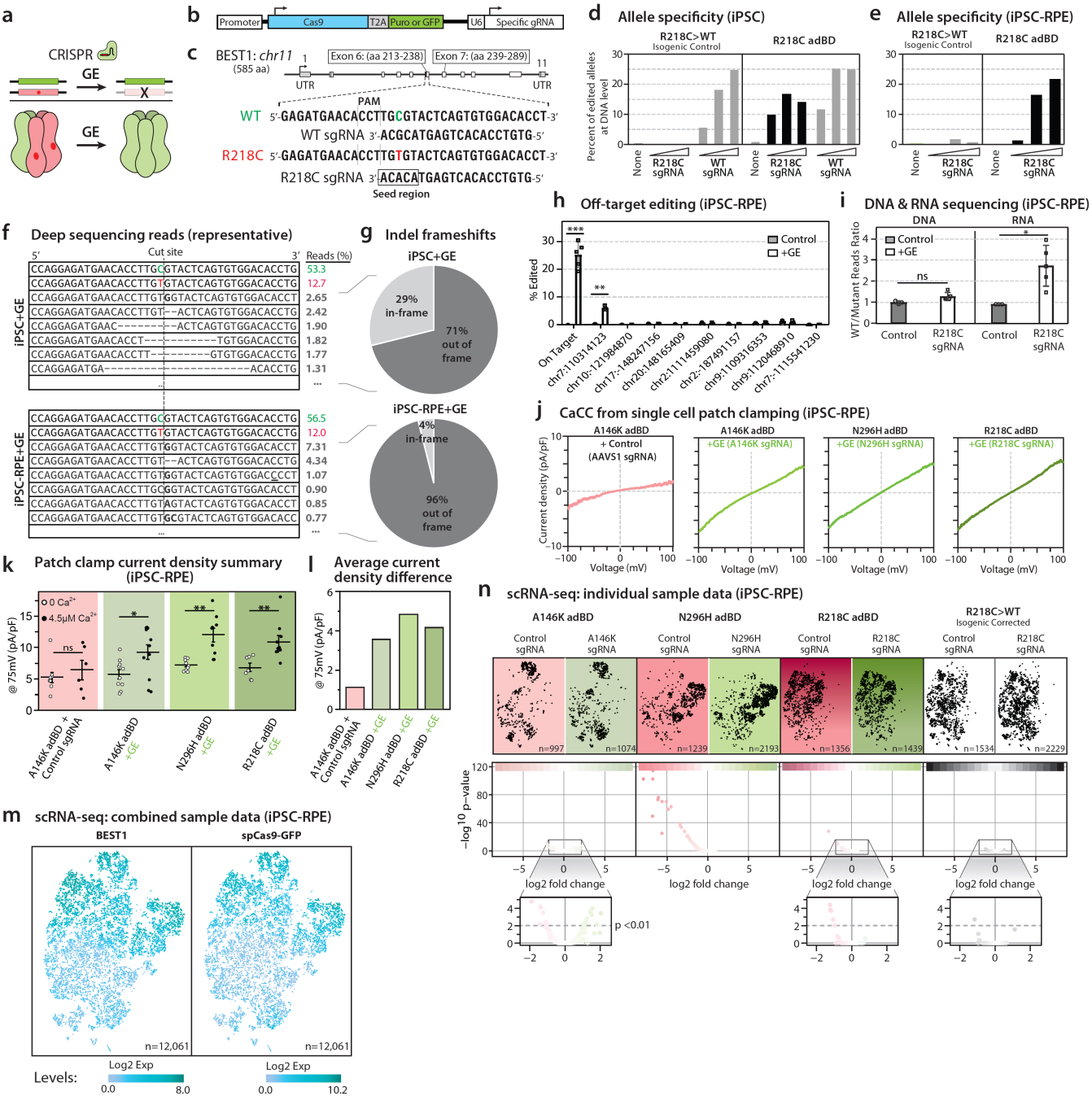

bioRxiv preprint doi: https://doi.org/10.1101/796581; this version posted October 10, 2019. The copyright holder for this preprint (which was not certified by peer review) is the author/funder, who has granted bioRxiv a license to display the preprint in perpetuity. It is made available under aCC-BY-NC 4.0 International license.

Figure 3 | Gene editing (GE) rescues CaCC activity in all adBD iPSC-RPE. (A) Rationale for using GE in adBD: introducing out-of-frame indels specifically in the MT *BEST1* allele via CRISPR/Cas9 targeting can silence its expression and restore normal WT BEST1 channel function. **(B)** LV construct used to express *sp*Cas9 and MT allele-targeted sgRNAs. **(C)** Diagram showing the heterozygous base pair substitution in R218C adBD (indicated in *red* and *green*) and design of the R218C and WT sgRNAs. **(D)** Percent of edited alleles in R218C>WT isogenic control iPSCs and R218C adBD iPSCs with increasing concentrations of WT sgRNA LV (single replicate at 0, 10, 100, or 500 µl dose). **(E)** Percent of edited alleles after treatment of R218C>WT isogenic control and R218C adBD iPSC-RPE with R218C sgRNA LV (single replicate at 0, 5, 50, or 150 µl dose). **(F)** Deep sequencing reads after treatment of R218C iPSC (*top*) or R218C iPSC-RPE (*bottom*) with R218C sgRNA LV and **(G)** corresponding calculated indel frameshift frequency for R218C iPSCs (*top*) and R218C iPSC-RPE (*bottom*). For panels f and g, data from a single representative example is shown; for additional replicates see **Supplemental Data File A**. **(H)** Frequency of edited alleles at on-target and top nine ranked off-target loci in iPSC-RPE treated with R218C sgRNA LV (n=3 for control and n=5 for +GE, except n=3 at *chr 7* locus). **(I)** Ratio of WT to MT allele DNA (*left*) and mRNA transcript reads (*right*) from R218C iPSC-RPE cultures treated with R218C sgRNA LV (n=5) or control LV (n=3 for *AAVS1* sgRNA and no sgRNA LV). **(J)** CaCC current density-voltage plots from single-cell patch clamp experiments of iPSC-RPE treated with MT allele-targeted sgRNA LV. For +calcium: n = 6 cells for *AAVS1*, n = 11 cells for A146K, n = 10 cells for R218C, n = 9 cells for N296H; for no calcium: n = 9 cells for *AAVS1*, n = 10 cells for A146K, n = 7 cells for R218C, n = 9 cells for N296H (data combined from two replicates). The number of cells from each replicate is listed in **Table S8**. **(K)** CaCC conductance for individual iPSC-RPE cells, and **(L)** mean CaCC conductance at 75 mV. The number of cells is the same as for panel j. **(M)** t-SNE plot of single iPSC-RPE cells across all 8 samples with relative expression of *BEST1* (*left*) and *spCas9-T2A-GFP* (*right*) depicted

bioRxiv preprint doi: https://doi.org/10.1101/796581; this version posted October 10, 2019. The copyright holder for this preprint (which was not certified by peer review) is the author/funder, who has granted bioRxiv a license to display the preprint in perpetuity. It is made available under aCC-BY-NC 4.0 International license.

via increasing shades of *blue*. Total number of cells analyzed (n) is shown. **(N)** *Top*, t-SNE plot of single cells (*black* dots) from each treated sample. Number of cells analyzed (n) for each sample is shown. *Bottom*, Volcano plots of transcriptome-wide differences in expression of individual genes (*red* or *green* dots) between iPSC-RPE of the same genotype treated with MT allele-targeted sgRNA (*green*) versus control (*AAVS1*, *red*) sgRNA LV. $p < 0.01$ was the threshold for determining significant versus non-significant changes in gene expression. Error bars in 3i represent mean ± SD; ns = $p \geq 0.05$, * for $p < 0.05$, ** for $p < 0.01$, *** for $p < 0.001$. Error bars in 3k represent mean ± SEM. See also Figures S4-S7.

bioRxiv preprint doi: https://doi.org/10.1101/796581; this version posted October 10, 2019. The copyright holder for this preprint (which was not certified by peer review) is the author/funder, who has granted bioRxiv a license to display the preprint in perpetuity. It is made available under aCC-BY-NC 4.0 International license.

343 **Figure S1. Related to Figures 1-2.**

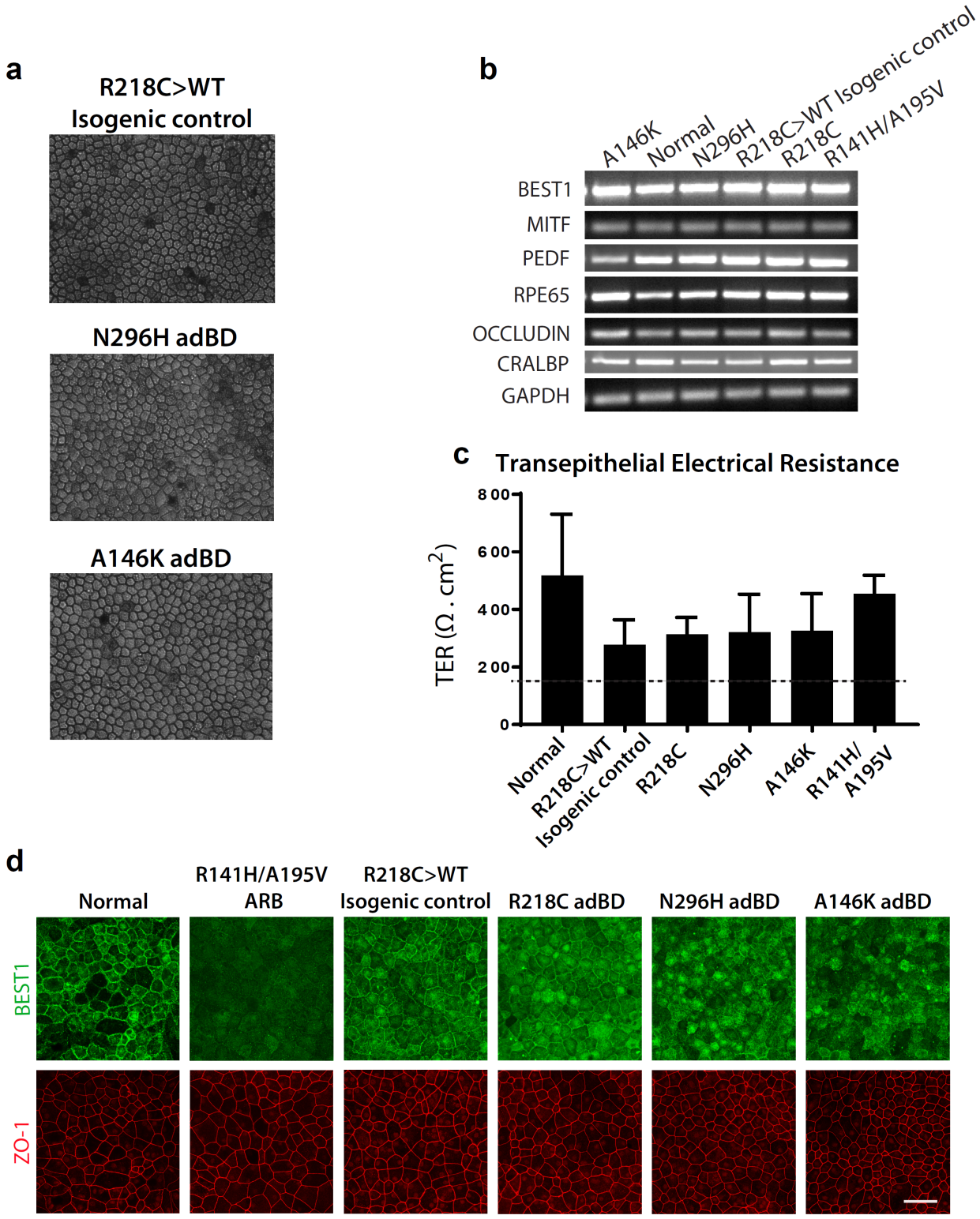

344

345

bioRxiv preprint doi: https://doi.org/10.1101/796581; this version posted October 10, 2019. The copyright holder for this preprint (which was not certified by peer review) is the author/funder, who has granted bioRxiv a license to display the preprint in perpetuity. It is made available under aCC-BY-NC 4.0 International license.

346 **Figure S1 | Characterization of iPSC-RPE. (A)** RPE differentiated from R218C>WT control iPSCs
347 (isogenic to the R218C adBD line) or patient-specific iPSCs harboring adBD mutations. **(B)** Gene
348 expression analysis (RT-PCR) of selected RPE-specific markers in all six lines. **(C)** Net transepithelial
349 electrical resistance (TER) ($\Omega \cdot cm^2$) for iPSC-RPE from all six lines. The dashed line demarcates the
350 minimum expected TER (150 $\Omega \cdot cm^2$). n=12 for each line (4 transwells from 3 replicates each), error bars
351 represent mean ± SD. **(D)** BEST1 and ZO-1 expression in iPSC-RPE. BEST1 expression level in
352 R141H/A195V ARB iPSC-RPE is reduced compared to other lines. BEST1 was visualized in the far-red
353 channel but was pseudo-colored green. Scale bar = 50 μM and applies to all images in panel d.

bioRxiv preprint doi: https://doi.org/10.1101/796581; this version posted October 10, 2019. The copyright holder for this preprint (which was not certified by peer review) is the author/funder, who has granted bioRxiv a license to display the preprint in perpetuity. It is made available under aCC-BY-NC 4.0 International license.

354 **Figure S2. Related to Figures 1-2.**

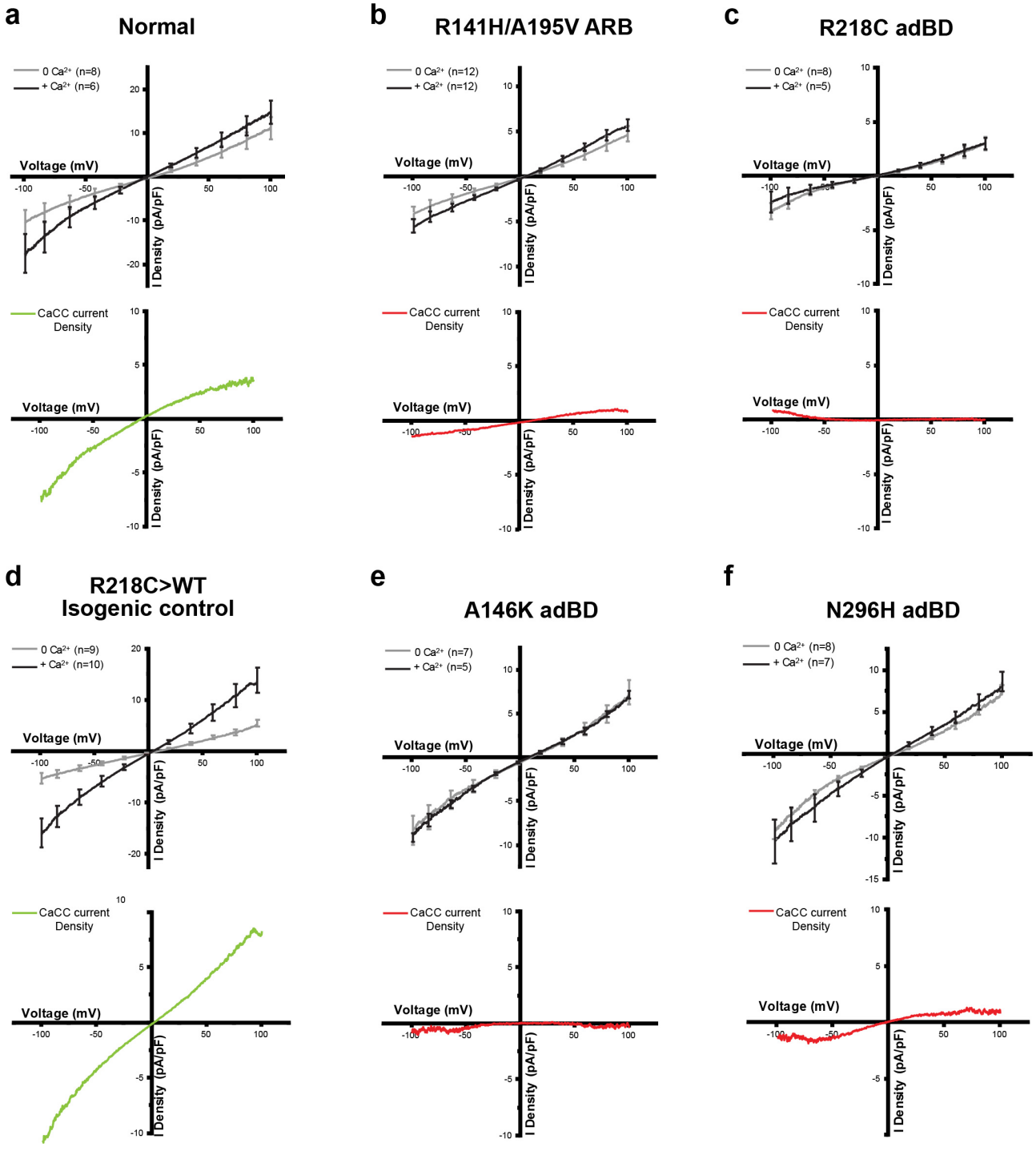

355

356

bioRxiv preprint doi: https://doi.org/10.1101/796581; this version posted October 10, 2019. The copyright holder for this preprint (which was not certified by peer review) is the author/funder, who has granted bioRxiv a license to display the preprint in perpetuity. It is made available under aCC-BY-NC 4.0 International license.

Figure S2 | Measurement of CaCC activity in WT, ARB, adBD, and gene-corrected iPSC-RPE. (A-C) Chloride current traces, measured in the presence (*black*) or absence (*gray*) of calcium over a voltage ramp (-100 to +100 mV), that were used to generate CaCC current density plots in Figure 1d (CaCC current density traces are also shown here for each panel). **(D-F)** Chloride current traces measured in the presence (*black*) or absence (*gray*) of calcium (*top*) and respective calculated CaCC current density traces (*bottom*) for R218C>WT isogenic control, A146K adBD, and N296H adBD iPSC-RPE. 4.5 μM calcium was used for +calcium conditions. *Green* traces denote normal, while *red* traces denote reduced CaCC current density. The number (n) of individual cells patch clamped in the presence or absence of calcium in order to calculate CaCC current densities is shown in the top left corner of each graph. Data were obtained from at least two replicates, and the n for each replicate is listed in **Table S8**.

bioRxiv preprint doi: https://doi.org/10.1101/796581; this version posted October 10, 2019. The copyright holder for this preprint (which was not certified by peer review) is the author/funder, who has granted bioRxiv a license to display the preprint in perpetuity. It is made available under aCC-BY-NC 4.0 International license.

367 **Figure S3. Related to Figures 1-2.**

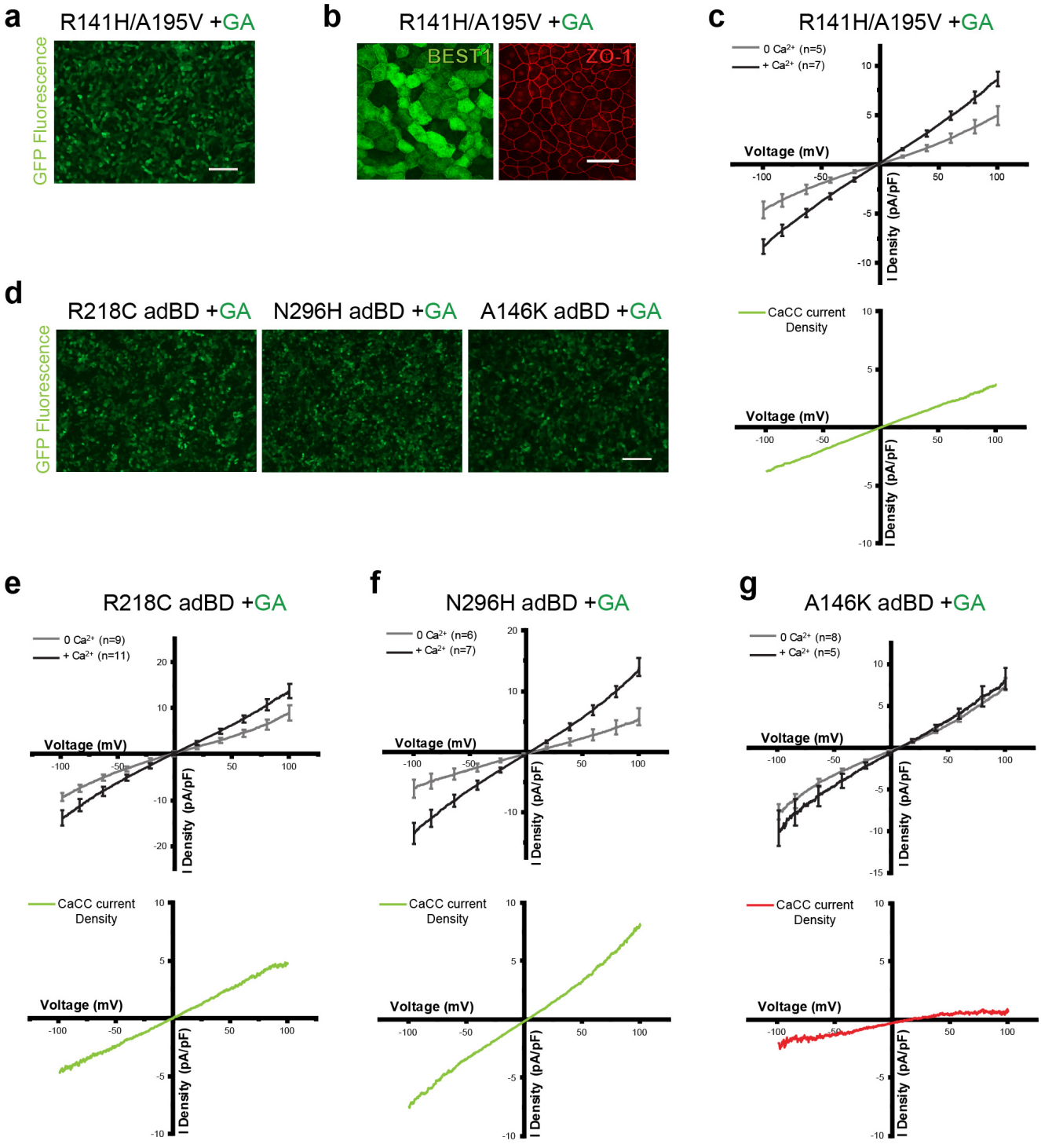

368

369

bioRxiv preprint doi: https://doi.org/10.1101/796581; this version posted October 10, 2019. The copyright holder for this preprint (which was not certified by peer review) is the author/funder, who has granted bioRxiv a license to display the preprint in perpetuity. It is made available under aCC-BY-NC 4.0 International license.

Figure S3 | GA restores CaCC function in ARB iPSC-RPE and N296H and R218C adBD iPSC-RPE, but not in A146K adBD iPSC-RPE. (A) GFP fluorescence in R141H/A195V ARB iPSC-RPE transduced with LV expressing hBEST1. Scale bar = 100 µm. **(B)** ICC analysis of BEST1 and ZO-1 expression in R141H/A195V iPSC-RPE transduced with LV expressing hBEST1. Increased BEST1 expression is observed in R141H/A195V +GA cells. Scale bar = 50 µm (applies to both images). **(C)** *Top*, Chloride current traces of R141H/A195V iPSC-RPE after GA measured in the presence (*black*) or absence (*gray*) of calcium. *Bottom*, Calculated CaCC current density trace for R141H/A195V iPSC-RPE after GA (also shown in Figure 2d). **(D)** GFP fluorescence in adBD iPSC-RPE transduced with LV expressing hBEST1. Scale bar = 100 µm (applies to all three images). **(E-G)** *Top*, Chloride current traces, measured in the presence (*black*) or absence (*gray*) of calcium over a voltage ramp (-100 to +100 mV), that were used to obtain CaCC current density plots (*bottom*; also shown in Figure 2g). 4.5 µM calcium was used for +calcium conditions. *Green* traces represent restored CaCC current densities, while *red* traces indicate no change. Cells with green fluorescence were used for all patch clamp measurements after GA. The number (n) of individual cells patch clamped in the presence or absence of calcium in order to calculate CaCC current densities is shown in the top left corner of each graph. Data were obtained from at least two replicates, and the n for each replicate is listed in **Table S8**.

bioRxiv preprint doi: https://doi.org/10.1101/796581; this version posted October 10, 2019. The copyright holder for this preprint (which was not certified by peer review) is the author/funder, who has granted bioRxiv a license to display the preprint in perpetuity. It is made available under aCC-BY-NC 4.0 International license.

387 **Figure S4, Related to Figure 3.**

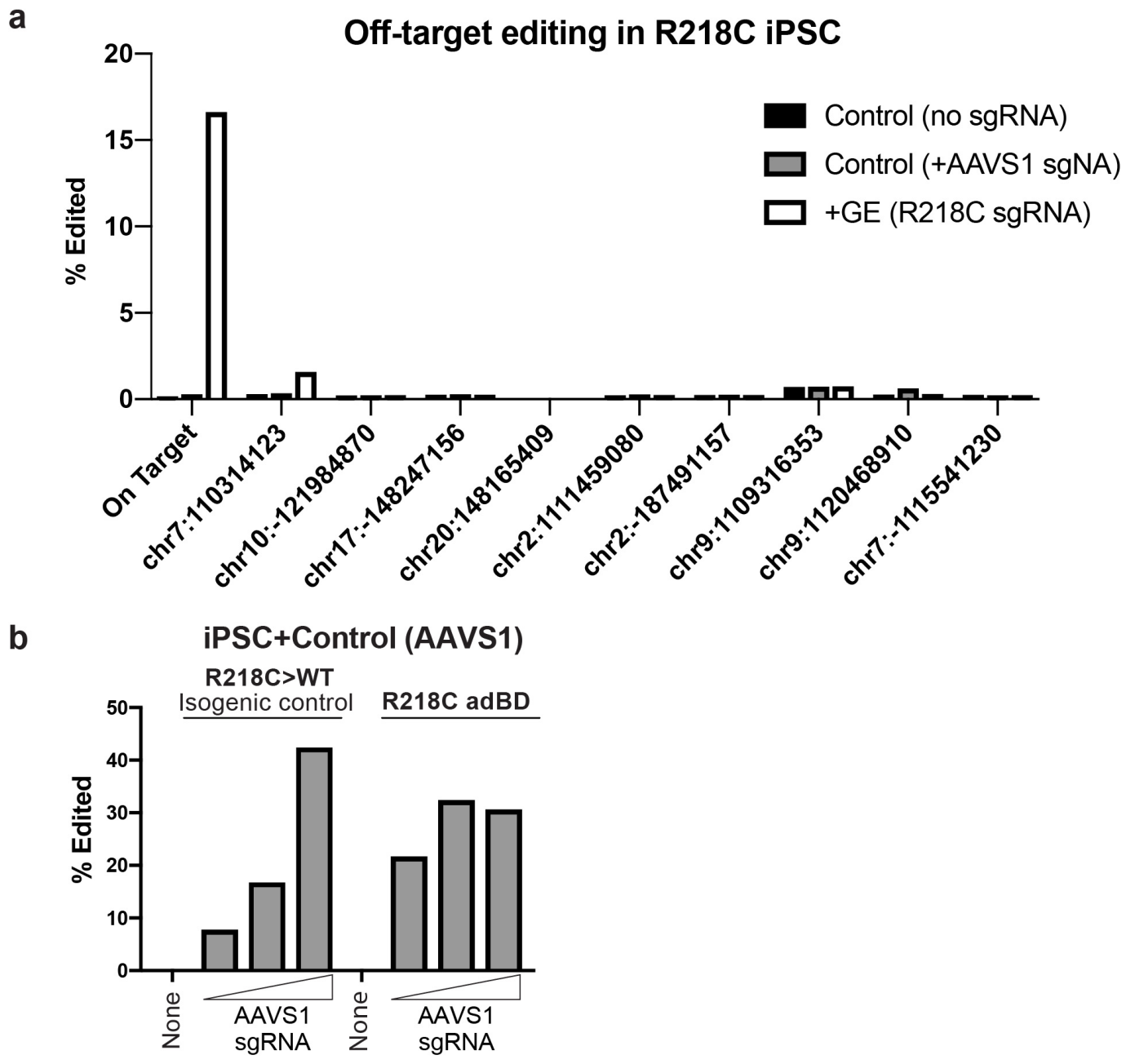

388

389

bioRxiv preprint doi: https://doi.org/10.1101/796581; this version posted October 10, 2019. The copyright holder for this preprint (which was not certified by peer review) is the author/funder, who has granted bioRxiv a license to display the preprint in perpetuity. It is made available under aCC-BY-NC 4.0 International license.

Figure S4 | Quantification of off-target editing and *AAVS*1 (control) editing in iPSCs. (A) Percent of alleles edited (% Edited) in R218C iPSCs at the on-target and top nine ranked off-target loci for the R218C sgRNA LV. Data presented are for a single sequencing replicate (n=1 each) of untreated R218C adBD iPSCs (no sgRNA) or R218C adBD iPSCs treated with LV encoding either R218C sgRNA or *AAVS1* sgRNA. **(B)** Percent of *AAVS1* alleles edited (% Edited) in R218C iPSCs and R218C>WT isogenic control iPSCs transduced with *AAVS1* sgRNA LV at 0, 10, 100, or 500 µl dose.

bioRxiv preprint doi: https://doi.org/10.1101/796581; this version posted October 10, 2019. The copyright holder for this preprint (which was not certified by peer review) is the author/funder, who has granted bioRxiv a license to display the preprint in perpetuity. It is made available under aCC-BY-NC 4.0 International license.

397 **Figure S5, Related to Figure 3.**

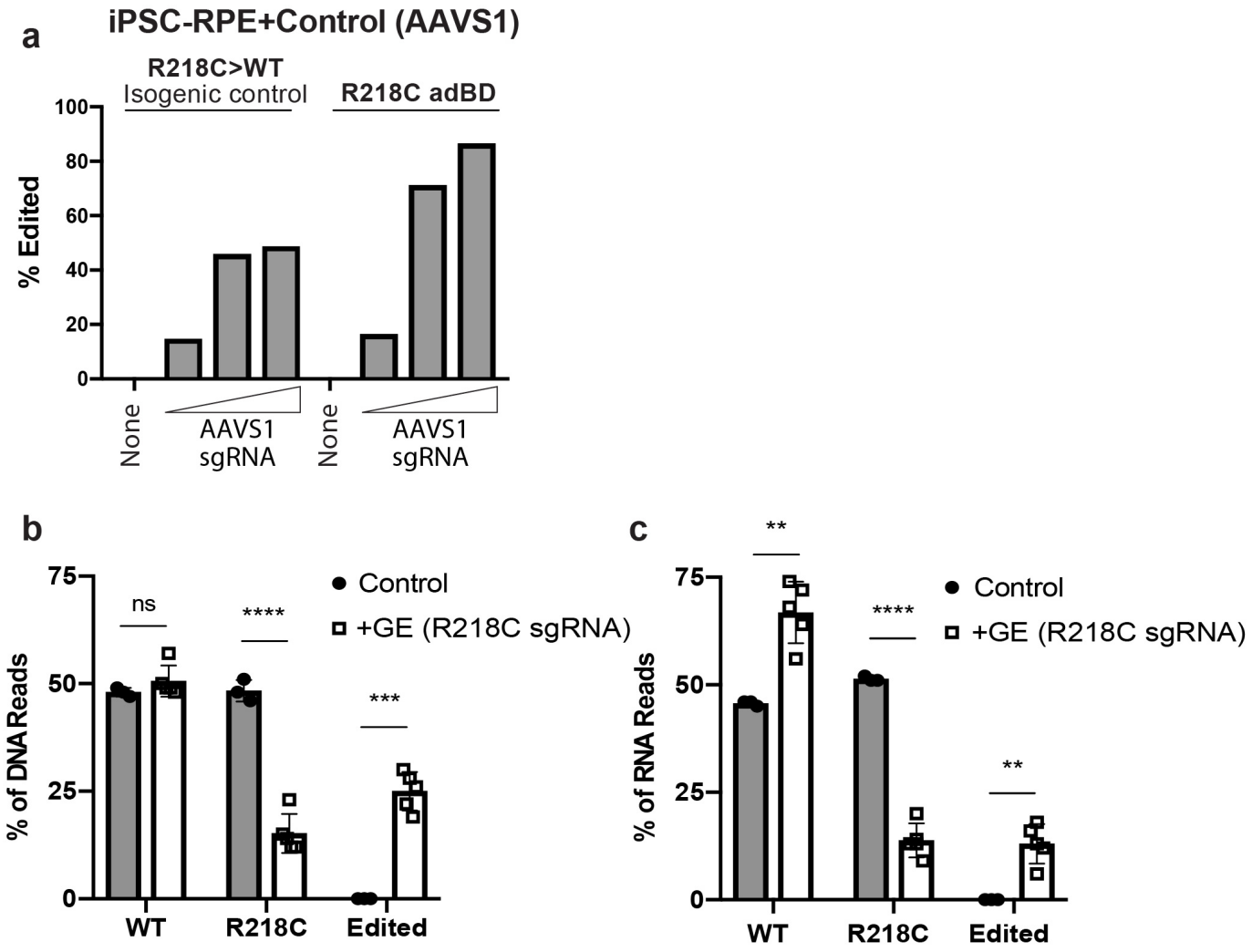

398

399

400 **Figure S5 | Quantification of DNA and RNA sequencing reads in GE iPSC-RPE. (A)** Percent of

401 *AAVS1* alleles edited (% Edited) in R218C adBD iPSC-RPE and R218C>WT isogenic control iPSC-RPE

402 transduced with *AAVS1* sgRNA LV at 0, 5, 50, or 150 µl dose. **(B)** Percent of WT, unedited R218C, or

403 edited DNA reads in R218C iPSC-RPE treated with R218C sgRNA or control (*AAVS1* sgRNA or no

404 sgRNA) LV shown in Figure 3i. **(C)** Percent of WT, unedited R218C, or edited RNA reads corresponding

405 to panel b and Figure 3i. Error bars represent mean ± SD; ns = $p \geq 0.05$, * for $p < 0.05$, ** for $p < 0.01$, ***

406 for $p < 0.001$, **** for $p < 0.0001$.

bioRxiv preprint doi: https://doi.org/10.1101/796581; this version posted October 10, 2019. The copyright holder for this preprint (which was not certified by peer review) is the author/funder, who has granted bioRxiv a license to display the preprint in perpetuity. It is made available under aCC-BY-NC 4.0 International license.

Figure S6, Related to Figure 3.

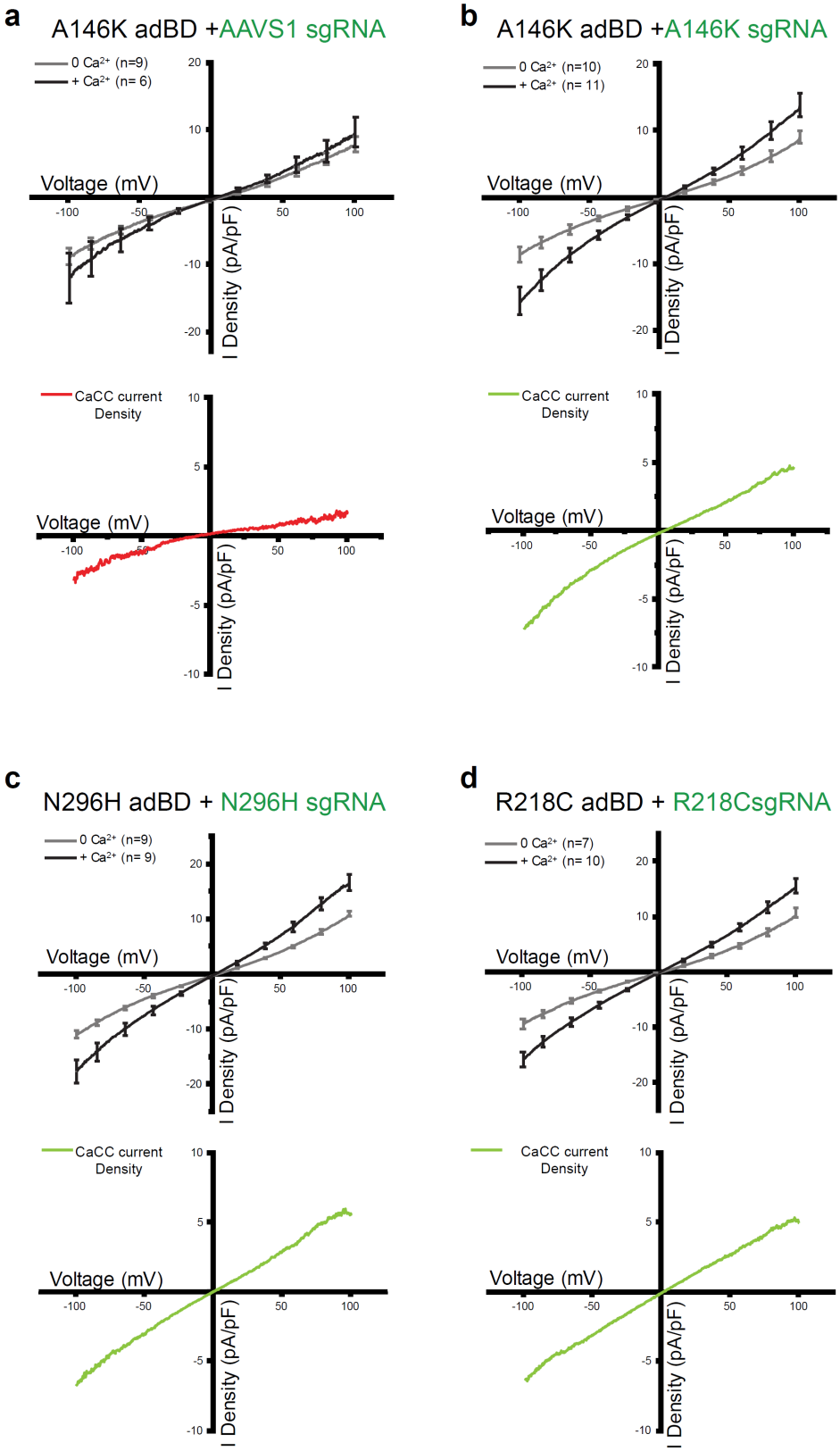

bioRxiv preprint doi: https://doi.org/10.1101/796581; this version posted October 10, 2019. The copyright holder for this preprint (which was not certified by peer review) is the author/funder, who has granted bioRxiv a license to display the preprint in perpetuity. It is made available under aCC-BY-NC 4.0 International license.

Figure S6 | GE restores CaCC activity in iPSC-RPE from all adBD lines. Chloride current traces (*top*), measured in the presence (*black*) or absence (*gray*) of calcium over a voltage ramp (-100 to +100 mV), that were used to calculate CaCC current density plots (*bottom*) after GE of iPSC-RPE from each adBD line. CaCC current density plots are also shown in Figure 3j. iPSC-RPE was edited using sgRNAs targeting **A,** *AAVS1* site in A146K adBD iPSC-RPE, **B,** A146K mutation in A146K adBD iPSC-RPE, **C,** N296H mutation in N296H adBD iPSC-RPE, or **D,** R218C mutation in R218C adBD iPSC-RPE. Cells with GFP fluorescence were used for whole cell patch clamp measurements and 4.5 μM calcium was used for +calcium conditions. *Red* traces denote reduced CaCC current density, while *green* traces denote restored CaCC function. The number (n) of individual cells patch clamped with or without calcium is shown at the top left corner of each graph. Data were obtained from two replicates, and the n for each replicate is listed in **Table S8**.

bioRxiv preprint doi: https://doi.org/10.1101/796581; this version posted October 10, 2019. The copyright holder for this preprint (which was not certified by peer review) is the author/funder, who has granted bioRxiv a license to display the preprint in perpetuity. It is made available under aCC-BY-NC 4.0 International license.

Figure S7, Related to Figure 3

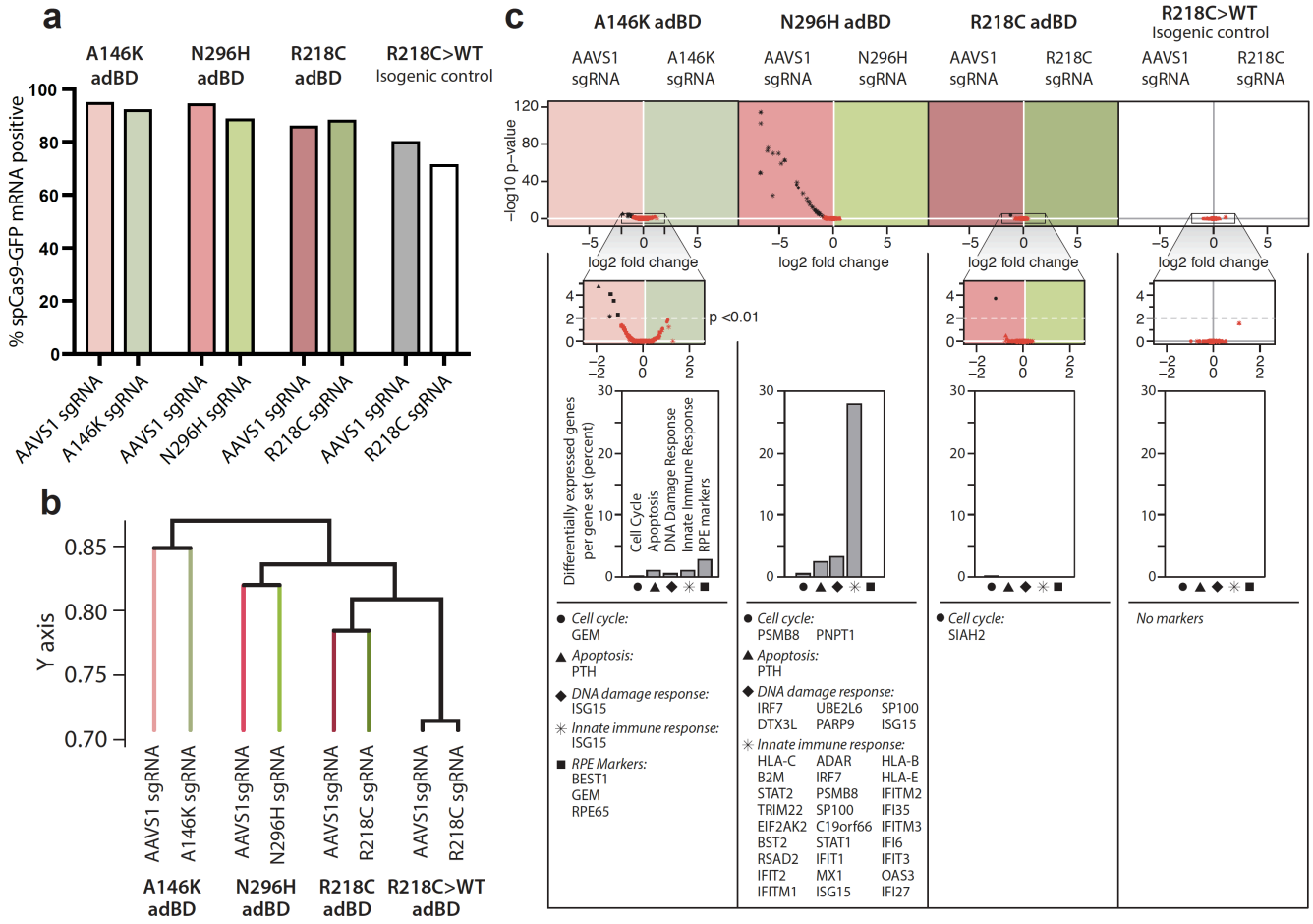

bioRxiv preprint doi: https://doi.org/10.1101/796581; this version posted October 10, 2019. The copyright holder for this preprint (which was not certified by peer review) is the author/funder, who has granted bioRxiv a license to display the preprint in perpetuity. It is made available under aCC-BY-NC 4.0 International license.

Figure S7 | Single-cell RNA-seq (scRNA-seq) analysis of iPSC-RPE after GE. (A) Percent of analyzed cells per sample for which *spCas9-T2A-GFP* transcripts were captured using scRNA-seq. **(B)** Dendrogram tree depicting relative similarity between samples. Non-negative matrix factorization-based gene cluster comparison across samples indicates that greater transcriptional variability exists between iPSC-RPE lines than between the same iPSC-RPE line treated with LV vectors encoding *sp*Cas9, GFP, or sgRNA (*AAVS1* sgRNA versus *BEST1* MT allele-targeted sgRNA). The dendrogram tree shows the similarity of the transcriptomes from each sample, derived from the average Jaccard coefficient between gene clusters from one sample and those from another sample. The y-axis denotes 1-average Jaccard coefficient and indicates the distance between different samples (tree tips) as well as between groups of samples (internal nodes). **(C)** Differential gene expression in 5 curated gene sets associated with cell cycle regulation (*circles*), apoptosis (*triangles*), DNA damage response (*diamonds*), innate immune response (*asterisks*), or RPE-identity (*squares*) in control (*AAVS1*) sgRNA versus MT allele-targeted sgRNA treated samples. For one sample pair (N296H iPSC-RPE), genes associated with a potential adverse treatment effect were upregulated in control sgRNA-treated sample compared to the MT allele-targeted sgRNA-treated sample.

bioRxiv preprint doi: https://doi.org/10.1101/796581; this version posted October 10, 2019. The copyright holder for this preprint (which was not certified by peer review) is the author/funder, who has granted bioRxiv a license to display the preprint in perpetuity. It is made available under aCC-BY-NC 4.0 International license.

STAR ★ METHODS

CONTACT FOR REAGENT AND RESOURCE SHARING

Further information and requests for resources and reagents should be directed to and will be fulfilled by the Lead Contact, David Gamm (dgamm@wisc.edu).

EXPERIMENTAL MODEL AND SUBJECT DETAILS

iPSC lines

A total of 6 iPSC lines, 2 control and 4 patient-specific, were used in this study. In addition to two adBD patient-specific iPSC lines previously used by our group for Best disease modeling (Singh et al., 2013b), we used three new iPSC lines (for detailed information on lines, including their characterization, please refer to **Table S1**). Two of the new iPSC lines harbored patient specific mutations: R218C for adBD and R141H/A195V for ARB. The ARB iPSC line was provided by Budd Tucker and Ed Stone (University of Iowa). One isogenic control iPSC line was obtained by CRISPR/Cas9-based gene correction of the patient-specific R218C adBD iPSC line (Steyer et al., 2018). All iPSC lines were cultured either on mouse embryonic fibroblasts (MEFs) or on Matrigel. Lines cultured on MEFs were maintained using iPS media (Dulbecco's Modified Eagle's Medium (DMEM)/F12 (1:1), 20% Knockout Serum Replacement (KOSR), 1% MEM non-essential amino acids, 1% L-glutamine, 0.2 mM β-mercaptoethanol, 100 ng/ml FGF-2), and iPSCs cultured on Matrigel were cultured with either mTeSR1 or StemFlex media. MEFs, FGF-2, and Matrigel were purchased from WiCell (Madison, WI). All other cell culture reagents were purchased from ThermoFisher Scientific. Karyotyping were performed as a quality control. The manuscript does not contain human subject or animal studies, and all work with iPSC

bioRxiv preprint doi: https://doi.org/10.1101/796581; this version posted October 10, 2019. The copyright holder for this preprint (which was not certified by peer review) is the author/funder, who has granted bioRxiv a license to display the preprint in perpetuity. It is made available under aCC-BY-NC 4.0 International license.

lines was carried out in accordance with institutional, national, and international guidelines and approved by the Stem Cell Research Oversight Committee at the University of Wisconsin-Madison.

METHOD DETAILS

Differentiation of iPSC lines to RPE

Differentiation of iPSCs to RPE was performed as previously described (Singh et al., 2013a; Singh et al., 2013b). Briefly, iPSCs were enzymatically lifted (1 mg/ml dispase for cells cultured on MEFs; 2 mg/ml dispase or 1 ml ReLeSR for cells cultured on Matrigel) to form aggregates, also referred to as embryoid bodies (EBs). EBs were maintained in suspension culture either in EB media (iPS media without FGF-2) and then switched to neural induction media (NIM) on day 4, or gradually weaned off mTeSR1/StemFlex and transitioned to NIM by day 4. NIM is composed of 500 ml DMEM/F12 (1:1), 1% N2 supplement, 1% MEM non-essential amino acids, 1% L-glutamine, 2 µg/ml heparin. EBs were plated on laminin (Cat# 23017015) coated 6-well plates (Nunc; Thermo Fisher Scientific) on day 7. On day 16, neural rosettes were mechanically lifted, leaving adherent cells behind that were maintained in retinal differentiation media (RDM; DMEM:F12 (3:1), 2% B27 without retinoic acid, 1% antibiotic-antimycotic solution). For the first four media changes, RDM was supplemented with 10 µM SU5402 and 3 µM CHIR99021.

After 60 days of differentiation, pigmented patches of RPE were micro-dissected, dissociated using Trypsin-EDTA (0.25%), and plated on laminin coated surfaces in RDM with 10% FBS and Rho kinase inhibitor (ROCKi; Y-27632). After 2 days, the media was changed to RDM with 2% FBS, and eventually to RDM once the cells were fully confluent. There were no differences observed between RPE differentiated from iPSCs cultured on MEFs and Matrigel. Mutant and wildtype genotypes of iPSC-RPE were verified by Sanger sequencing periodically. Heparin (Cat# H-3149) and SU5402 (Cat# SML0443-

bioRxiv preprint doi: https://doi.org/10.1101/796581; this version posted October 10, 2019. The copyright holder for this preprint (which was not certified by peer review) is the author/funder, who has granted bioRxiv a license to display the preprint in perpetuity. It is made available under aCC-BY-NC 4.0 International license.

485 25MG) were from Sigma-Aldrich, CHIR99021 (Cat# 4423) was from Tocris Bioscience, and ReLeSR
486 was purchased from STEMCELL Technologies. All other differentiation reagents were purchased from
487 ThermoFisher Scientific.
488
489 **Gene expression analysis**
490 Reverse transcriptase-PCR was used to assess RPE-specific gene expression in RPE derived from
491 different iPSC lines as described previously (Singh et al., 2013b). Primers used are listed in **Table S2**.
492
493 **Generation of lentiviral (LV) vectors**
494 LV plasmid with the human *VMD2* promoter driving expression of *hBEST1-T2A-GFP* was
495 provided by Alfred S. Lewin (University of Florida). LentiCRISPR v2 (LCv2) plasmid was purchased
496 from Addgene (Cat# 52961), and molecular cloning was used to insert specific sgRNA sequences (**Table**
497 **S5**) as described (Steyer et al., 2018). LV plasmids for GE containing specific sgRNA sequences and the
498 human *VMD2* promoter driving expression of *spCas9-T2A-GFP* (**Table S3**) were then generated as
499 described hereafter (all primers used are listed in **Table S4**). To begin, the '*T2A-GFP-WPRE*' sequence
500 was amplified from the *hVMD2-hBEST1-T2A-GFP* plasmid using LCv2-GFP.Gib.F and .R primers and
501 Q5 2X MM (NEB, Cat# M0492L). The '*2A-Puro-WPRE*' sequence was then removed from the LCv2
502 plasmid via restriction digestion with PmeI (NEB, Cat# R0560S) and BamHI (NEB, Cat# R3136S). The
503 digestion product was resolved on a 0.7% agarose gel and the plasmid backbone was purified using the
504 Monarch gel purification kit (NEB, Cat# T1020S). The '*T2A-GFP-WPRE*' sequence was inserted into the
505 digested backbone using the Gibson Assembly kit (SGI, Cat# GA1100) per the manufacturer's
506 instructions. The completed Gibson Assembly reaction was then amplified using chemically competent *E.*
507 *coli* (NEB, Cat# C3040H) and Sanger sequenced to confirm insertion of '*T2A-GFP-WPRE*' using LCv2-

bioRxiv preprint doi: https://doi.org/10.1101/796581; this version posted October 10, 2019. The copyright holder for this preprint (which was not certified by peer review) is the author/funder, who has granted bioRxiv a license to display the preprint in perpetuity. It is made available under aCC-BY-NC 4.0 International license.

GFP.seq.L and LCv2-GFP.seq.R primers. This intermediate plasmid product (*pLCv2-GFP*) was digested with AfeI (NEB, Cat# R0652S) and EcoRI-HF (NEB, Cat R310S) to remove the constitutive EF-1 alpha core promoter. The desired digestion product was purified as described above. The *hVMD2* promoter was then PCR amplified from *hVMD2-hBEST1-T2A-GFP* using Q5 2X MM and VMD2.LCv2.GFP.Gib.F and .R primers, followed by insertion into the digested LCv2-GFP backbone via Gibson Assembly. Next, the completed Gibson reaction was transformed into chemically competent *E. coli* and the sequence of the final product *hVMD2-spCas9-T2A-GFP* was confirmed via Sanger sequencing using VMD2.LCv2.GFP.seq.L and .R primers. Subsequently, specific sgRNAs were cloned into *hVMD2-spCas9-T2A-GFP* using the same restriction digest and Gibson Assembly protocol described for generation of the LCv2 GE vectors.

LV production and cell transduction

LV stocks were generated by the Cell Culture Core of the UW Department of Dermatology Skin Disease Research Center (Madison, WI). Briefly, HEK293 cells cultured on 10-cm dishes were transfected with LV plasmids—10 µg of sgRNA encoding LV plasmid (*hVMD2-hBEST1-T2A-GFP, hVMD2-spCas9-T2A-GFP* or LCv2); 5 µg of psPax2 (Addgene, Cat# 12260), and 2 µg of pMD2.G (Addgene, Cat# 12259)—using Lipofectamine (ThermoFisher; Cat# 11668019). After 15 hours, culture medium (DMEM with 10% FBS) was replaced with fresh media containing 1% Penicillin-Streptomycin. Media containing LV was collected the next day and viral titers (**Table S6**) were calculated using QuickTiter Lentivirus Titer Kit (Cell Biolabs, Cat# VPK-107).

For iPSC transduction, iPSCs between passages 10-30 were cultured on Matrigel (Corning, Cat #354230) coated plates in StemFlex (Gibco, Cat#A3349401) medium. Cells were then seeded at 15,000 cells/well on Matrigel-coated 48-well plates, and 48 hours post-seeding they were transduced with LV

bioRxiv preprint doi: https://doi.org/10.1101/796581; this version posted October 10, 2019. The copyright holder for this preprint (which was not certified by peer review) is the author/funder, who has granted bioRxiv a license to display the preprint in perpetuity. It is made available under aCC-BY-NC 4.0 International license.

containing LCv2 encoding *AAVS1*, R218C, or WT sgRNA at a dose of 0, 10, 100, or 500 µl. StemFlex medium was then added to a total volume of 750 µl per well. 48 hours after LV treatment, the media was replaced with 250 µl of fresh StemFlex. At 96 hours after LV treatment, total genomic DNA was harvested and analyzed via sequencing as described under the 'Deep sequencing analysis of DNA and RNA read frequency' section.

For iPSC-RPE transduction, monolayers of iPSC-RPE on transwells were treated with 0, 5, 50, or 150 µl (Figure 3e) or 150 µl alone (GA experiments and Figures 3h, 3i) of specified LV preparation. Media was changed on day 2 to RDM, and cells were maintained in culture with media changes every 3 days until used for sequencing or other analyses.

Transepithelial electrical resistance (TER) measurements

Monolayers of RPE cultured on transwell inserts (Corning, #3470) were used for all TER measurements. To perform the measurements, we employed an epithelial voltohmmeter (EVOM2) with chopstick electrodes (STX2) from World Precision Instruments (Sarasota, USA) according to manufacturer's instructions. Electrodes were sterilized with ethanol, and then rinsed in sterile Milli-Q water followed by HBSS before measuring electrical resistance of RPE monolayers. Differences between TER values of transwells with cultured RPE monolayers versus background measurements of cell-free transwell inserts were multiplied by the surface area of the transwell membrane to obtain net TER values in $\Omega \cdot cm^2$.

CaCC current density measurements

All iPSC-RPE cells used for chloride current measurements were cultured as a monolayer on transwells. To singularize cells prior to measurement, transwells were washed twice with 0 Na-CMF

bioRxiv preprint doi: https://doi.org/10.1101/796581; this version posted October 10, 2019. The copyright holder for this preprint (which was not certified by peer review) is the author/funder, who has granted bioRxiv a license to display the preprint in perpetuity. It is made available under aCC-BY-NC 4.0 International license.

554 solution (135 mM N-Methyl-D-glucamine (NMDG)-Cl, 5 mM KCl, 10 mM HEPES, 10 mM glucose, 2
555 mM EDTA-KOH, pH adjusted to 7.4) and then incubated with papain enzyme solution (0 Na-CMF
556 solution containing 2.5 µl/ml papain (46 mg/ml, MP Biomedicals LLC, Cat#100921), 0.375 mg/ml
557 adenosine, 0.3mg/ml L-cysteine, 0.25 mg/ml L- glutathione, and 0.05mg/ ml taurine) for 30 minutes at
558 37^{o}C/5% CO_2. To stop the reaction, 0.01% BSA was added to the enzymatic solution. After washing
559 twice with 0 Na-CMF solution, cells were dispersed in extracellular solution containing 140 mM NaCl, 10
560 mM HEPES, 3 mM KCl, 2 mM $CaCl_2$, 2 mM $MgCl_2$, and 5.5 mM glucose adjusted to pH 7.4 with NaOH
561 by gentle pipetting.

562 Cells with polarized RPE morphology post-dissociation (**Figure 2b**, *left*) were used to measure
563 chloride currents. To test effects of GA or GE on *BEST1* mutant iPSC-RPE by single-cell patch clamp
564 analysis, only cells with GFP fluorescence (from transduction with *hVMD2-hBEST1-T2A-GFP* for GA or
565 *hVMD2-spCas9-T2A-GFP* encoding *AAVS1* sgRNA or MT allele-targeted sgRNAs for GE) were used.
566 Current recordings on these cells were performed using the conventional whole-cell patch clamp
567 technique with an Axopatch 200A amplifier controlled by Clampex software program via the digidata
568 1550 data acquisition system (Axon Instruments, CA). Fire-polished borosilicate glass pipettes with 3-5
569 MΩ resistance were filled with pipette solution containing 4.5 µM calcium or no calcium.

570 Recordings were carried out at room temperature and current-voltage tracings were established
571 using ramps from -100 to +100 mV for 1000 ms. The pipette solution with calcium was comprised of (in
572 mM) 146 CsCl, 5 (Ca^{2+})-EGTA-NMDG, 2 $MgCl_2$, 8 HEPES, and 10 sucrose at pH 7.3, adjusted with
573 NMDG. Another pipette solution devoid of calcium was comprised of (in mM) 146 CsCl, 5 EGTA-
574 NMDG, 2 $MgCl_2$, 8 HEPES, and 10 Sucrose at pH 7.3, adjusted with NMDG. Both of these pipette
575 solutions were mixed to make the solution containing 4.5 µM free calcium as described
576 previously(Kuruma and Hartzell, 2000), which was then used for patch clamping.

bioRxiv preprint doi: https://doi.org/10.1101/796581; this version posted October 10, 2019. The copyright holder for this preprint (which was not certified by peer review) is the author/funder, who has granted bioRxiv a license to display the preprint in perpetuity. It is made available under aCC-BY-NC 4.0 International license.

577 Current density values were obtained by dividing current amplitude with cell capacitance
578 measurements. CaCC current densities for iPSC-RPE are represented as differences between mean 4.5
579 µM calcium response and mean no calcium response from a total of at least five cells for each condition.
580 At least two differentiations were used as replicates to obtain data for each line.
581
582 **Immunocytochemistry**
583 iPSC-RPE cultured on transwell inserts were washed with PBS and fixed with 4%
584 paraformaldehyde for 10 minutes at room temperature (RT). After washing fixed cells three times with
585 PBS, transwell membranes were placed in blocking solution (10% normal donkey serum with 5% BSA,
586 1% fish gelatin and 0.5% Triton-X100 in PBS) for one hour at RT, and then incubated overnight at 4 ^{o}C
587 in primary antibody (1:100 mouse anti-Bestrophin (Millipore, Cat# MAB5466); 1:100 rabbit anti-ZO-1
588 (ThermoFisher Scientific, Cat# 61-7300)) prepared in blocking solution. Cells were then washed three
589 times in PBS and incubated for 30 minutes at RT in appropriate secondary antibody (ThermoFisher
590 Scientific; 1:500 Donkey anti-Mouse IgG (Cat# A31571); 1:500 Donkey anti-Rabbit IgG (Cat# A10040))
591 prepared in blocking solution. Cells were again washed three times in PBS, incubated in DAPI (1:500;
592 ThermoFisher; Cat# D1306) for 30 minutes, mounted using prolong gold with DAPI (ThermoFisher; Cat#
593 P36931), and imaged using Nikon A1R confocal microscope with NIS Elements AR 5.0 software.
594
595 **Photoreceptor outer segment (POS) phagocytosis and rhodopsin degradation assay**
596 POS feeding of iPSC-RPE was performed as described previously (Singh et al., 2013b). Briefly, bovine
597 POS (InVision BioResources (Seattle, WA)) were gently resuspended in DMEM. 100 µl media was then
598 removed from each transwell insert, $6.25x10^{6}$ POS were added, and cells were incubated at 37 ^{o}C and 5%
599 CO_2 for 2 hours. Afterward, POS containing RDM was removed and each transwell was washed

bioRxiv preprint doi: https://doi.org/10.1101/796581; this version posted October 10, 2019. The copyright holder for this preprint (which was not certified by peer review) is the author/funder, who has granted bioRxiv a license to display the preprint in perpetuity. It is made available under aCC-BY-NC 4.0 International license.

thoroughly three times using DPBS. Following the washes, cells were harvested (0 time point) or further incubated in fresh RDM for prescribed periods of time. At each time point, transwells were washed, 100 µl RIPA buffer (ThermoFisher; Cat# 89900) containing protease inhibitor cocktail (Sigma-Aldrich; Cat# P8340) was added, and cells were incubated on ice for 30 minutes to extract total cell protein. Protein quantification was performed using the DC Protein assay kit II (Bio-Rad, Cat# 5000112).

Western blots were then performed to monitor rhodopsin degradation as described(Singh et al., 2015; Singh et al., 2013b). Briefly, protein lysates were denatured in 1X Laemmli buffer (reducing) and kept on ice for 10 minutes. Protein samples were then separated on 4-20% mini-Protean TGX gels (Bio-Rad; Cat# 4568095) and electroblotted onto PVDF membranes (Millipore; IPFL10100). After blotting, membranes were dried at RT for 15 minutes, re-activated in methanol for 1 minute, and then incubated in blocking buffer (1:1 Odyssey blocking buffer (LI-COR Biosciences; Cat# 927-40000):PBS) for 1 hour. Post-blocking, blots were incubated in primary antibodies (1:500 mouse anti-rhodopsin (Millipore, Cat# MABN15); 0.1 µg/ml rabbit anti-beta actin (Abcam, Cat# ab8227)) in blocking buffer with 0.1% Tween-20 overnight, washed three times for 5 minutes each in PBS with 0.1% Tween-20, incubated for 1.5 hours at RT in appropriate secondary antibody (LI-COR Biosciences; 1:20,000 Donkey anti-Rabbit IgG (Cat# 926-32213); 1:20,000 Donkey anti-Mouse IgG (Cat# 926-68022)) in blocking buffer with 0.1% Tween-20 and 0.01% SDS, and then washed three times for 5 minutes each in PBS with 0.1% Tween-20. An Odyssey infrared Imager (LI-COR Biosciences) was used to image blots using Image Studio software. ImageJ was used for quantification of relevant protein bands.

Deep sequencing analysis of DNA and RNA read frequency

Cells were singularized with TrypLE Express (Gibco, Cat# 12605010) per manufacturer's instructions. Total DNA and/or RNA was extracted using QuickExtract DNA (Epicentre, Cat# QE09050)

bioRxiv preprint doi: https://doi.org/10.1101/796581; this version posted October 10, 2019. The copyright holder for this preprint (which was not certified by peer review) is the author/funder, who has granted bioRxiv a license to display the preprint in perpetuity. It is made available under aCC-BY-NC 4.0 International license.

623 or QuickExtract RNA (Epicentre, Cat# QER090150), respectively. Both DNA and RNA extractions were
624 performed per manufacturer's instructions with the following minor modifications: 1) a ratio of 10,000-
625 25,000 cells per 50 µl of QuickExtract solution was routinely used, and 2) an optional DNase 1 treatment
626 was omitted from the RNA extraction protocol. All samples were stored at -80 ºC until use.
627 RNA was reverse transcribed to cDNA using the ProtoScript II First Strand synthesis kit (NEB, Cat#
628 E6560S) and synthesis was performed with the "random primer" option included within the kit. 4 µl of
629 crude RNA extract was added to each cDNA reaction.
630 In preparation for targeted deep sequencing, Illumina adapter sequences and sample-specific
631 barcodes were appended to genomic or cDNA amplicons via overhang PCR as described(Steyer et al.,
632 2018).
633 Purified amplicon libraries were assembled into 2 nM total DNA in DNAse/RNAse free H_2O and
634 sequenced using 150 nucleotide paired end reads using MiSeq (6M or 15M total reads) at the UW Biotech
635 Center (Madison, WI) with the following loading condition: 8 pmol total DNA and 15% PhiX DNA.
636 Raw FASTQ files were read and aligned to expected amplicons using a command line implementation of
637 CRISPResso (v1.0.8)(Pinello et al., 2016). Full commands used for analysis are provided in the Source
638 Data for each corresponding Supplemental Figure panel. 'Percent allele identity' or 'percent edited' were
639 determined using the software's standard output table of individual read identities. Sequencing reads with
640 counts <100 were not included in the analysis. All FASTQ files are available upon request.
641
642 **Single-cell RNA sequencing (scRNA-seq)**
643 iPSC-RPE cultures from the A146K, N296H, and R218C adBD patient lines and an isogenic
644 gene-corrected control line derived from the R218C line (R218C>WT) were transduced with 150 µl of
645 *hVMD2-spCas9-T2A-GFP* encoding specific sgRNAs as described in the 'LV production and cell

bioRxiv preprint doi: https://doi.org/10.1101/796581; this version posted October 10, 2019. The copyright holder for this preprint (which was not certified by peer review) is the author/funder, who has granted bioRxiv a license to display the preprint in perpetuity. It is made available under aCC-BY-NC 4.0 International license.

646 transduction' section. For each sample, sgRNAs were either targeted to mutant *BEST1* or to the *AAVS1*
647 locus (control). On day 14, cells were dissociated from transwells with a papain dissociation kit
648 (Worthington Biochemical, Cat# LK003150) and filtered using a Flowmi cell strainer (Bel-Art SP
649 Scienceware, Cat# H13680-0040) to obtain single-cell suspension. Cells were then prepared for scRNA-
650 seq with the droplet-based 10X Genomics GemCode platform according to the manufacturer's
651 instructions. In brief, singularized cells were encapsulated in oil beads containing a unique molecular
652 identifier (UMI) barcode. The cells were then lysed and cDNA libraries were created featuring cell and
653 transcript-specific molecular identifiers. Libraries were sequenced using an Illumina HiSeq2500 Rapid
654 Run and reads were aligned to a custom reference genome consisting of the human hg19 GRCh38
655 genome and an added gene for the *spCas9-T2A-GFP* transcript.
656
657 **scRNA-seq data analysis**
658 Genome edited iPSC-RPE were clustered based on their genome-wide transcriptome using the t-
659 Distributed Stochastic Neighbor Embedding (t-SNE) algorithm with the 10X Genomics Loupe Cell
660 Browser software (v2.0.0). Reads for each pair of samples (*BEST1* mutant allele-targeted sgRNA vs
661 *AAVS1* sgRNA control) were aligned, analyzed, clustered with Cell Ranger v2.1.1, and compared to
662 detect significant differences in gene expression, with p values adjusted using the Benjamini-Hochberg
663 correction for multiple tests. $P < 0.01$ was used as the significance threshold for all analyses. Cell Ranger
664 using the aggregate feature was run to concatenate each pair of samples with the same genotype, and
665 differential gene expression within each pair (with gene editing at either the *AAVS1* or *BEST1* locus) was then
666 analyzed. Potential adverse events were probed using gene lists curated from gene ontology terms
667 associated with the cell cycle, apoptosis, DNA damage response, and the innate immune response, as well
668 as a list of 149 validated marker genes associated with human RPE(Strunnikova et al., 2010)

bioRxiv preprint doi: https://doi.org/10.1101/796581; this version posted October 10, 2019. The copyright holder for this preprint (which was not certified by peer review) is the author/funder, who has granted bioRxiv a license to display the preprint in perpetuity. It is made available under aCC-BY-NC 4.0 International license.

669 (**Supplemental Data File C**; gene ontology sets are available on the Molecular Signatures Database
670 <http://software.broadinstitute.org/gsea/msigdb>). Differentially-expressed genes with p <0.01 were
671 deemed to be significant. All significantly differentially-expressed genes per cluster are reported, with the
672 exception of genes identified by Cell Ranger as having low average UMI counts. Volcano plots were generated
673 in RStudio (v.1.1.456) using the ggplot2 package.
674
675 **Non-negative matrix factorization-based comparison of scRNA-seq datasets**
676 Non-negative matrix factorization (NMF) followed by clustering of genes using the NMF factors was
677 used for **Figure S7B** to project each dataset into a gene group. The input data for this analysis were a set of
678 gene barcode matrices generated using the Cell Ranger 2.1.1 algorithm. The matrices were filtered to remove
679 background barcodes in order to include only detected cellular barcodes, and then further filtered to exclude
680 cells expressing fewer than 2000 total counts, followed by depth normalization.
681 To enable comparison of transcriptional signatures from each sample, NMF(Lee and Seung, 2000)
682 was applied to each scRNA-seq dataset. NMF is a popular dimensionality reduction and clustering
683 approach that is used to project data into low dimensional non-negative factors, and thus can be used to
684 derive a clustering of cells and genes. NMF with k=10 factors was applied with a total of five NMF runs.
685 Next, the similarity of NMF results was compared between two samples using the average best Jaccard
686 coefficient between clusters of one versus another sample. 1-average Jaccard coefficient was then used as
687 the distance to apply hierarchical clustering on the samples. This procedure was repeated five times and
688 the tree that appeared most often was used. The trees learned in different iterations were largely similar
689 and always grouped the patient-specific lines first before grouping different lines together.
690
691 **QUANTIFICATION AND STATISTICAL ANALYSIS**

bioRxiv preprint doi: https://doi.org/10.1101/796581; this version posted October 10, 2019. The copyright holder for this preprint (which was not certified by peer review) is the author/funder, who has granted bioRxiv a license to display the preprint in perpetuity. It is made available under aCC-BY-NC 4.0 International license.

692 Unless otherwise specified, all analyses were performed using GraphPad Prism (v.8.0.1) and error
693 bars represent mean ± SD; ns = $p \geq 0.05$, * for $p < 0.05$, ** for $p < 0.01$, *** for $p < 0.001$, **** for p
694 < 0.0001. Further detail for each analysis is provided here. Statistical analyses for Figures 2i and 3k were
695 performed using Origin 2018b. Student's *t*-test was performed to measure the significance between the
696 groups. P values < 0.05 were considered statistically significant. Statistical significance for Figure 3h and 3i
697 was determined using the Holm-Sidak method with alpha = 0.05. Each row was analyzed individually, without
698 assuming a consistent SD (number of *t* tests = 10 and 2 for Figure 3h, and 3i, respectively). Statistical
699 significance for differential gene expression in Figures 3n and Figure S7c was determined using the Cell
700 Ranger 2.1.1 algorithm. Sample pairs with each genotype were analyzed and clustered with individual Cell
701 Ranger runs for each pair and analyzed using the Loupe Cell Browser (v.2.0.0). Differential expression was
702 calculated using a negative binomial exact test, and p values were adjusted using the Benjamini-Hochberg
703 correction for multiple tests. $P < 0.01$ was used as the threshold for assigning significant versus non-
704 significant changes in gene expression. Volcano plots were generated in RStudio (v 1.1.456) using the
705 ggplot2 package. For Figures S5B and S5C, discovery was determined using the two-stage linear step-up
706 procedure of Benjamini, Krieger, and Yekutieli with Q = 1%. Each row was analyzed individually, without
707 assuming a consistent SD (number of *t* tests = 3).
708

709 **DATA AND SOFTWARE AVAILABILITY**

710 Upon acceptance, scRNA-seq data will be posted to an accession database. Raw targeted
711 sequencing files for DNA and RNA sequencing data will be deposited to the NCBI Trace and Short-Read
712 Archive. Raw patch clamp data are available upon request. All other experimental data are provided in the
713 source data files or in Supplemental data.
714

bioRxiv preprint doi: https://doi.org/10.1101/796581; this version posted October 10, 2019. The copyright holder for this preprint (which was not certified by peer review) is the author/funder, who has granted bioRxiv a license to display the preprint in perpetuity. It is made available under aCC-BY-NC 4.0 International license.

715 **REFERENCES**

716 Bakondi, B., Lv, W.J., Lui, B., Jones, M.K., Tsai, Y., Kim, K.J., Levy, R., Akhtar, A.A., Breunig, J.J.,
717 Svendseni, C.N., *et al*. (2016). In Vivo CRISPR/Cas9 Gene Editing Corrects Retinal Dystrophy in the
718 S334ter-3 Rat Model of Autosomal Dominant Retinitis Pigmentosa. Mol Ther *24*, 556-563.

719

720 Boon, C.J.F., Klevering, B.J., Leroy, B.P., Hoyng, C.B., Keunen, J.E.E., and den Hollander, A.I. (2009).
721 The spectrum of ocular phenotypes caused by mutations in the BEST1 gene. Prog Retin Eye Res *28*, 187-
722 205.

723

724 Courtney, D.G., Moore, J.E., Atkinson, S.D., Maurizi, E., Allen, E.H., Pedrioli, D.M., McLean, W.H.,
725 Nesbit, M.A., and Moore, C.B. (2016). CRISPR/Cas9 DNA cleavage at SNP-derived PAM enables both
726 in vitro and in vivo KRT12 mutation-specific targeting. Gene Ther *23*, 108-112.

727

728 Cox, D.B., Platt, R.J., and Zhang, F. (2015). Therapeutic genome editing: prospects and challenges. Nat
729 Med *21*, 121-131.

730

731 Cromer, M.K., Vaidyanathan, S., Ryan, D.E., Curry, B., Lucas, A.B., Camarena, J., Kaushik, M., Hay,
732 S.R., Martin, R.M., Steinfeld, I., *et al*. (2018). Global Transcriptional Response to CRISPR/Cas9-AAV6-
733 Based Genome Editing in CD34(+) Hematopoietic Stem and Progenitor Cells. Mol Ther *26*, 2431-2442.

734

735 Cukras, C., Wiley, H.E., Jeffrey, B.G., Sen, H.N., Turriff, A., Zeng, Y., Vijayasarathy, C., Marangoni, D.,
736 Ziccardi, L., Kjellstrom, S., *et al*. (2018). Retinal AAV8-RS1 Gene Therapy for X-Linked Retinoschisis:
737 Initial Findings from a Phase I/IIa Trial by Intravitreal Delivery. Mol Ther *26*, 2282-2294.

bioRxiv preprint doi: https://doi.org/10.1101/796581; this version posted October 10, 2019. The copyright holder for this preprint (which was not certified by peer review) is the author/funder, who has granted bioRxiv a license to display the preprint in perpetuity. It is made available under aCC-BY-NC 4.0 International license.

Dickson, V.K., Pedi, L., and Long, S.B. (2014). Structure and insights into the function of a Ca2+-activated Cl- channel. Nature *516*, 213-218.

Doudna, J.A., and Charpentier, E. (2014). The new frontier of genome engineering with CRISPR-Cas9. Science *346*, 1077-+.

George, A.L., Jr. (2004). Inherited Channelopathies Associated with Epilepsy. Epilepsy Curr *4*, 65-70.

Guziewicz, K.E., Cideciyan, A.V., Beltran, W.A., Komaromy, A.M., Dufour, V.L., Swider, M., Iwabe, S., Sumaroka, A., Kendrick, B.T., Ruthel, G., *et al*. (2018). BEST1 gene therapy corrects a diffuse retina-wide microdetachment modulated by light exposure. P Natl Acad Sci USA *115*, E2839-E2848.

Guziewicz, K.E., Sinha, D., Gomez, N.M., Zorych, K., Dutrow, E.V., Dhingra, A., Mullins, R.F., Stone, E.M., Gamm, D.M., Boesze-Battaglia, K., *et al*. (2017). Bestrophinopathy: An RPE-photoreceptor interface disease. Prog Retin Eye Res *58*, 70-88.

Johnson, A.A., Guziewicz, K.E., Lee, C.J., Kalathur, R.C., Pulido, J.S., Marmorstein, L.Y., and Marmorstein, A.D. (2017). Bestrophin 1 and retinal disease. Prog Retin Eye Res *58*, 45-69.

Kuruma, A., and Hartzell, H.C. (2000). Bimodal control of a Ca(2+)-activated Cl(-) channel by different Ca(2+) signals. J Gen Physiol *115*, 59-80.

bioRxiv preprint doi: https://doi.org/10.1101/796581; this version posted October 10, 2019. The copyright holder for this preprint (which was not certified by peer review) is the author/funder, who has granted bioRxiv a license to display the preprint in perpetuity. It is made available under aCC-BY-NC 4.0 International license.

761 Kuscu, C., Arslan, S., Singh, R., Thorpe, J., and Adli, M. (2014). Genome-wide analysis reveals
762 characteristics of off-target sites bound by the Cas9 endonuclease. Nat Biotechnol *32*, 677-683.
763 Lam, B.L., Davis, J.L., Gregori, N.Z., MacLaren, R.E., Girach, A., Verriotto, J.D., Rodriguez, B., Rosa,
764 P.R., Zhang, X., and Feuer, W.J. (2019). Choroideremia Gene Therapy Phase 2 Clinical Trial: 24-Month
765 Results. Am J Ophthalmol *197*, 65-73.
766
767 Ledford, H. (2017). FDA advisers back gene therapy for rare form of blindness. Nature *550*, 314.
768
769 Lee, D.D., and Seung, H.S. (2000). Algorithms for Non-negative Matrix Factorization. Advances in
770 Neural Information Processing Systems *13*, 556-562.
771
772 Li, P., Kleinstiver, B.P., Leon, M.Y., Prew, M.S., Navarro-Gomez, D., Greenwald, S.H., Pierce, E.A.,
773 Joung, J.K., Liu, Q. (2018). Allele-Specific CRISPR-Cas9 Genome Editing of the Single-Base P23H
774 Mutation for Rhodopsin-Associated Dominant Retinitis Pigmentosa. The CRISPR Journal *1*, 55-64.
775
776 Li, Y., Zhang, Y., Xu, Y., Kittredge, A., Ward, N., Chen, S., Tsang, S.H., and Yang, T. (2017). Patient-
777 specific mutations impair BESTROPHIN1's essential role in mediating Ca(2+)-dependent Cl(-) currents
778 in human RPE. Elife *6*.
779
780 Mali, P., Yang, L., Esvelt, K.M., Aach, J., Guell, M., DiCarlo, J.E., Norville, J.E., and Church, G.M.
781 (2013). RNA-guided human genome engineering via Cas9. Science *339*, 823-826.
782

bioRxiv preprint doi: https://doi.org/10.1101/796581; this version posted October 10, 2019. The copyright holder for this preprint (which was not certified by peer review) is the author/funder, who has granted bioRxiv a license to display the preprint in perpetuity. It is made available under aCC-BY-NC 4.0 International license.

783 Milenkovic, A., Milenkovic, V.M., Wetzel, C.H., and Weber, B.H.F. (2018). BEST1 protein stability and
784 degradation pathways differ between autosomal dominant Best disease and autosomal recessive
785 bestrophinopathy accounting for the distinct retinal phenotypes. Hum Mol Genet *27*, 1630-1641.
786
787 Pattanayak, V., Lin, S., Guilinger, J.P., Ma, E., Doudna, J.A., and Liu, D.R. (2013). High-throughput
788 profiling of off-target DNA cleavage reveals RNA-programmed Cas9 nuclease specificity. Nat Biotechnol
789 *31*, 839-843.
790
791 Pawan K. Shahi, D.H., Divya Sinha, Simran Brar, Hannah Moulton, Sabrina Stulo, Katarzyna D. Borys,
792 Elizabeth Capowski, De-Ann M. Pillers, David M. Gamm, Bikash R. Pattnaik (2019). Gene augmentation
793 and read-through rescue channelopathy in an iPSC-RPE model of congenital blindness. American Journal
794 of Human Genetics.
795
796 Pinello, L., Canver, M.C., Hoban, M.D., Orkin, S.H., Kohn, D.B., Bauer, D.E., and Yuan, G.C. (2016).
797 Analyzing CRISPR genome-editing experiments with CRISPResso. Nat Biotechnol *34*, 695-697.
798
799 Popp, M.W., and Maquat, L.E. (2016). Leveraging Rules of Nonsense-Mediated mRNA Decay for
800 Genome Engineering and Personalized Medicine. Cell *165*, 1319-1322.
801
802 Russell, S., Bennett, J., Wellman, J.A., Chung, D.C., Yu, Z.F., Tillman, A., Wittes, J., Pappas, J., Elci, O.,
803 McCague, S., *et al*. (2017). Efficacy and safety of voretigene neparvovec (AAV2-hRPE65v2) in patients
804 with RPE65-mediated inherited retinal dystrophy: a randomised, controlled, open-label, phase 3 trial.
805 Lancet *390*, 849-860.

bioRxiv preprint doi: https://doi.org/10.1101/796581; this version posted October 10, 2019. The copyright holder for this preprint (which was not certified by peer review) is the author/funder, who has granted bioRxiv a license to display the preprint in perpetuity. It is made available under aCC-BY-NC 4.0 International license.

Sadelain, M., Papapetrou, E.P., and Bushman, F.D. (2011). Safe harbours for the integration of new DNA in the human genome. Nat Rev Cancer *12*, 51-58.

Schaaf, C.P. (2014). Nicotinic acetylcholine receptors in human genetic disease. Genet Med *16*, 649-656.

Shen, M.W., Arbab, M., Hsu, J.Y., Worstell, D., Culbertson, S.J., Krabbe, O., Cassa, C.A., Liu, D.R., Gifford, D.K., and Sherwood, R.I. (2018). Predictable and precise template-free CRISPR editing of pathogenic variants. Nature *563*, 646-651.

Singh, R., Kuai, D., Guziewicz, K.E., Meyer, J., Wilson, M., Lu, J., Smith, M., Clark, E., Verhoeven, A., Aguirre, G.D., *et al*. (2015). Pharmacological Modulation of Photoreceptor Outer Segment Degradation in a Human iPS Cell Model of Inherited Macular Degeneration. Mol Ther *23*, 1700-1711.

Singh, R., Phillips, M.J., Kuai, D., Meyer, J., Martin, J.M., Smith, M.A., Perez, E.T., Shen, W., Wallace, K.A., Capowski, E.E., *et al*. (2013a). Functional analysis of serially expanded human iPS cell-derived RPE cultures. Invest Ophthalmol Vis Sci *54*, 6767-6778.

Singh, R., Shen, W., Kuai, D., Martin, J.M., Guo, X.R., Smith, M.A., Perez, E.T., Phillips, M.J., Simonett, J.M., Wallace, K.A., *et al*. (2013b). iPS cell modeling of Best disease: insights into the pathophysiology of an inherited macular degeneration. Hum Mol Genet *22*, 593-607.

bioRxiv preprint doi: https://doi.org/10.1101/796581; this version posted October 10, 2019. The copyright holder for this preprint (which was not certified by peer review) is the author/funder, who has granted bioRxiv a license to display the preprint in perpetuity. It is made available under aCC-BY-NC 4.0 International license.

827 Steyer, B., Bu, Q., Cory, E., Jiang, K., Duong, S., Sinha, D., Steltzer, S., Gamm, D., Chang, Q., and Saha,
828 K. (2018). Scarless Genome Editing of Human Pluripotent Stem Cells via Transient Puromycin Selection.
829 Stem Cell Reports *10*, 642-654.
830
831 Strunnikova, N.V., Maminishkis, A., Barb, J.J., Wang, F., Zhi, C., Sergeev, Y., Chen, W., Edwards, A.O.,
832 Stambolian, D., Abecasis, G., *et al*. (2010). Transcriptome analysis and molecular signature of human
833 retinal pigment epithelium. Hum Mol Genet *19*, 2468-2486.
834
835 Tsai, Y.T., Wu, W.H., Lee, T.T., Wu, W.P., Xu, C.L., Park, K.S., Cui, X., Justus, S., Lin, C.S., Jauregui,
836 R., *et al*. (2018). Clustered Regularly Interspaced Short Palindromic Repeats-Based Genome Surgery for
837 the Treatment of Autosomal Dominant Retinitis Pigmentosa. Ophthalmology *125*, 1421-1430.
838
839 Vasireddy, V., Mills, J.A., Gaddameedi, R., Basner-Tschakarjan, E., Kohnke, M., Black, A.D.,
840 Alexandrov, K., Zhou, S., Maguire, A.M., Chung, D.C., *et al*. (2013). AAV-mediated gene therapy for
841 choroideremia: preclinical studies in personalized models. PLoS One *8*, e61396.
842
843 Villa, C., and Combi, R. (2016). Potassium Channels and Human Epileptic Phenotypes: An Updated
844 Overview. Front Cell Neurosci *10*, 81.
845
846 Waugh, N., Loveman, E., Colquitt, J., Royle, P., Yeong, J.L., Hoad, G., and Lois, N. (2018). Treatments
847 for dry age-related macular degeneration and Stargardt disease: a systematic review. Health Technol
848 Assess *22*, 1-168.
849

bioRxiv preprint doi: https://doi.org/10.1101/796581; this version posted October 10, 2019. The copyright holder for this preprint (which was not certified by peer review) is the author/funder, who has granted bioRxiv a license to display the preprint in perpetuity. It is made available under aCC-BY-NC 4.0 International license.

Wienert, B., Shin, J., Zelin, E., Pestal, K., and Corn, J.E. (2018). In vitro-transcribed guide RNAs trigger an innate immune response via the RIG-I pathway. PLoS Biol *16*, e2005840.

Yang, T., Liu, Q., Kloss, B., Bruni, R., Kalathur, R.C., Guo, Y., Kloppmann, E., Rost, B., Colecraft, H.M., and Hendrickson, W.A. (2014). Structure and selectivity in bestrophin ion channels. Science *346*, 355-359.

bioRxiv preprint doi: https://doi.org/10.1101/796581; this version posted October 10, 2019. The copyright holder for this preprint (which was not certified by peer review) is the author/funder, who has granted bioRxiv a license to display the preprint in perpetuity. It is made available under aCC-BY-NC 4.0 International license.

SUPPLEMENTAL DATA

Data Figures (attached below**):**

Data S1. R141H/A195V ARB iPSC line characterization.

Data S2. Western blots for rhodopsin degradation assays.

Supplemental Tables (attached below**):**

Table S1. List of iPSC lines used and their subsequent characterization.

Table S2: RPE-specific RT-PCR primers used.

Table S3. List of GE vectors used.

Table S4. List of primers for lentiviral plasmid generation.

Table S5. List of sgRNAs.

Table S6. Lentivirus titers.

Table S7. Primers for deep sequencing of DNA and cDNA.

Table S8. Number of cells used for CaCC current density measurements.

Supplemental Data Files (available for download**):**

Supplemental Data File A. Replicates for frameshift analysis of iPSC+GE versus iPSC-RPE+GE.

Supplemental Data File B. Comparison of experimental indel frequency outcomes in iPSC-RPE+GE versus outcomes predicted by the inDelphi tool.

Supplemental Data File C. Curated gene sets used to assess differences in gene expression between control (*AAVS1*) and MT *BEST1* allele-targeted sgRNA in Figure S7C.

Supplemental Data File D. Ranked off-target sites for sgRNAs used in this study.

bioRxiv preprint doi: https://doi.org/10.1101/796581; this version posted October 10, 2019. The copyright holder for this preprint (which was not certified by peer review) is the author/funder, who has granted bioRxiv a license to display the preprint in perpetuity. It is made available under aCC-BY-NC 4.0 International license.

DATA FIGURES

Data S1. R141H/A195V ARB iPSC line characterization.

Karyotype

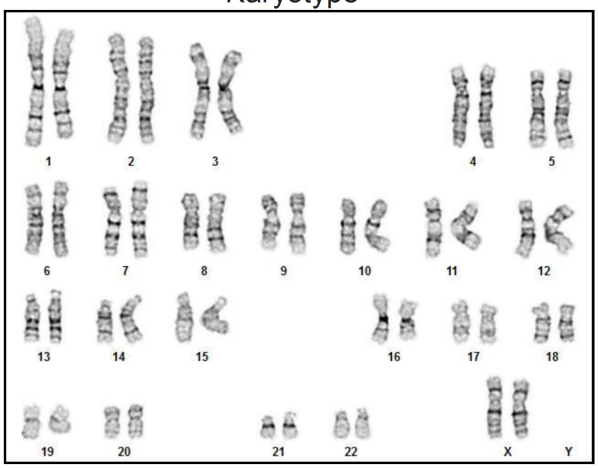

R141H mutation*

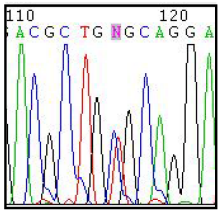

A195V mutation

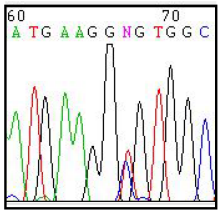

*Complementary DNA sequence

Pluripotency analysis

Self-renewal		
Gene	P10	P22
CXCL5	3.78	3.34
DNMT3B	0.12	0.13
HESX1	0.14	0.17
IDO1	1.23	1.38
LCK	0.84	0.60
NANOG	1.60	1.43
POU5F1	0.30	0.27
SOX2	1.09	1.12
TRIM22	2.64	2.36
Average	**1.30**	**1.20**

Fold change legend	
fc > 100	Upregulated
10 < fc <= 100	
2 < fc <= 10	
0.5 <= fc <= 2	Comparable
0.1 <= fc < 0.5	
0.01 <= fc <0.1	
fc < 0.01	Downregulated

Ectoderm markers		
Target Name	P10	P22
CDH9	1.52	2.13
COL2A1	3.07	2.73
DMBX1	2.13	3.03
DRD4	0.14	0.22
EN1	0.20	0.23
LMX1A	0.07	0.20
MAP2	1.41	0.97
MYO3B	0.97	0.81
NOS2	0.31	0.31
NR2F1/NR2F2	0.00	0.00
NR2F2	0.04	0.12
OLFM3	0.16	0.15
PAPLN	1.07	0.92
PAX3	0.02	0.02
PAX6	0.02	0.05
POU4F1	0.04	0.19
PRKCA	0.30	0.36
SDC2	9.64	8.17
SOX1	0.10	0.05
TRPM8	0.45	0.35
WNT1	0.71	0.92
ZBTB16	0.13	0.08

Mesoendoderm markers		
Target Name	P10	P22
FGF4	0.29	0.25
GDF3	1.26	0.87
NPPB	0.00	0.00
NR5A2	44.39	34.18
PTHLH	0.29	0.38
T	0.00	0.00

Mesoderm markers		
Target Name	P10	P22
ABCA4	1.11	1.29
ALOX15	0.20	0.21
BMP10	0.03	0.02
CDH5	0.35	0.27
CDX2	0.07	0.05
COLEC10	1.33	1.50
ESM1	0.01	0.01
FCN3	0.62	0.48
FOXF1	0.27	0.27
HAND1	0.01	0.01
HAND2	0.09	0.25
HEY1	1.39	0.79
HOPX	0.31	3.27
IL6ST	0.81	0.65
NKX2-5	0.16	0.18
ODAM	0.02	0.02
PDGFRA	0.16	0.14
PLVAP	0.41	0.36
RGS4	0.10	0.09
SNAI2	0.18	0.25
TBX3	0.01	0.01
TM4SF1	0.08	0.06
CXCL5	3.78	3.34
DNMT3B	0.12	0.13
HESX1	0.14	0.17
IDO1	1.23	1.38
LCK	0.84	0.60
NANOG	1.60	1.43
POU5F1	0.30	0.27
SOX2	1.09	1.12
TRIM22	2.64	2.36

Endoderm markers		
Target Name	P10	P22
AFP	0.00	0.00
CABP7	0.14	0.24
CDH20	0.12	0.16
CLDN1	0.50	0.46
CPLX2	0.07	0.05
ELAVL3	0.38	0.48
EOMES	0.02	0.02
FOXA1	0.00	0.00
FOXA2	0.00	0.00
FOXP2	0.41	0.34
GATA4	0.02	0.01
GATA6	0.00	0.01
HHEX	0.23	0.25
HMP19	0.27	0.37
HNF1B	0.04	0.02
HNF4A	0.01	0.00
KLF5	0.49	0.51
LEFTY1	0.04	0.01
LEFTY2	0.05	0.03
NODAL	0.07	0.05
PHOX2B	0.01	0.01
POU3F3	0.02	0.00
PRDM1	0.16	0.20
RXRG	0.09	0.07
SOX17	0.00	0.00
SST	0.16	0.10

bioRxiv preprint doi: https://doi.org/10.1101/796581; this version posted October 10, 2019. The copyright holder for this preprint (which was not certified by peer review) is the author/funder, who has granted bioRxiv a license to display the preprint in perpetuity. It is made available under aCC-BY-NC 4.0 International license.

Data S2. Western blots for rhodopsin degradation assays.

Blots used for POS degradation graphs in Figure 2e (boxes represent areas used for quantification).
Boxed area was selected to include bands corresponding to fully denatured rhodopsin and its aggregated forms.

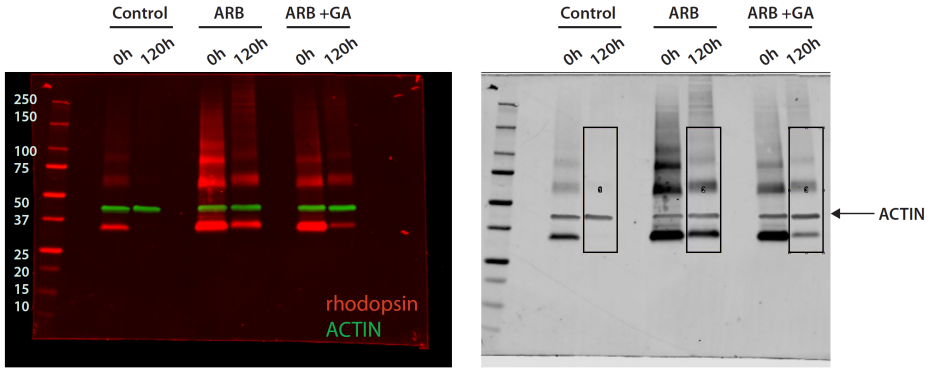

Blots used for POS degradation graphs in Figure 2h (boxes represent areas used for quantification).

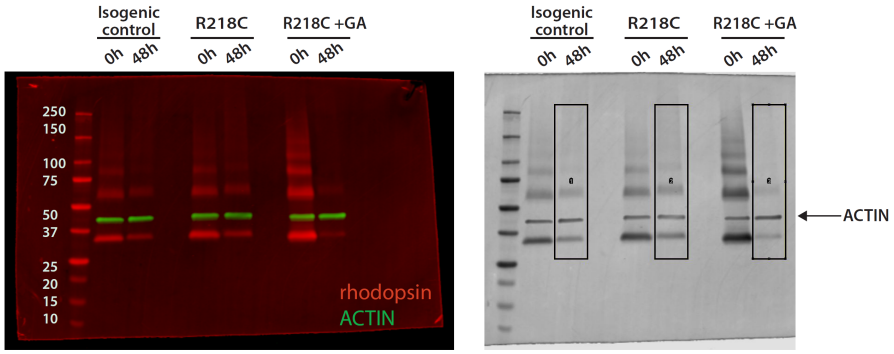

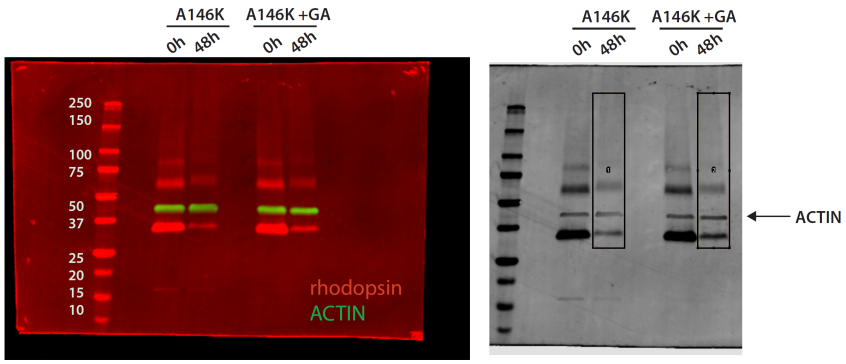

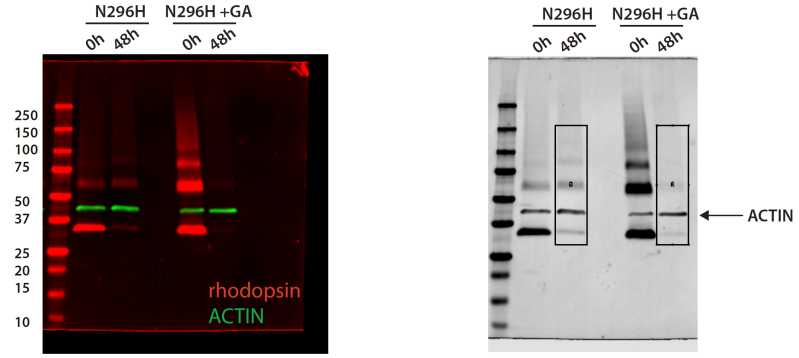

bioRxiv preprint doi: https://doi.org/10.1101/796581; this version posted October 10, 2019. The copyright holder for this preprint (which was not certified by peer review) is the author/funder, who has granted bioRxiv a license to display the preprint in perpetuity. It is made available under aCC-BY-NC 4.0 International license.

SUPPLEMENTAL TABLES

Table S1. List of iPSC lines used and their subsequent characterization.

iPSC line	*BEST1* Genotype	Karyotype	Pluripotency Confirmation	Reference
Normal	WT/WT	Yes	Yes	Singh et al., Hum Mol Genet., 2013
R218C>WT Isogenic Control	WT/WT (isogenic to R218C/WT adBD iPSC line)	Yes	Yes	Steyer et al., Stem Cell Reports, 2018
R218C adBD	R218C/WT	Yes	Yes	Steyer et al., Stem Cell Reports, 2018
N296H adBD	N296H/WT	Yes	Yes	Singh et al., Hum Mol Genet., 2013
A146K adBD	A146K/WT	Yes	Yes	Singh et al., Hum Mol Genet., 2013
R141H/A195V ARB	R141H/A195V	Yes	Yes	Data S1

bioRxiv preprint doi: https://doi.org/10.1101/796581; this version posted October 10, 2019. The copyright holder for this preprint (which was not certified by peer review) is the author/funder, who has granted bioRxiv a license to display the preprint in perpetuity. It is made available under aCC-BY-NC 4.0 International license.

890 **Table S2: RPE-specific RT-PCR primers used.**
891

Gene	**Forward Primer**	**Reverse Primer**
BEST1	ATTTATAGGCTGGCCCTCACGGAA	TGTTCTGCCGGAGTCATAAAGCCT
MITF	TTCACGAGCGTCCTGTATGCAGAT	TTGCAAAGCAGGATCCATCAAGCC
PEDF	AATCCATCATTCACCGGGCTCTCT	TGCACCCAGTTGTTGATCTCTTGC
RPE65	GCCCTCCTGCACAAGTTTGACTTT	AGTTGGTCTCTGTGCAAGCGTAGT
OCCLUDIN	TCATTGCCGCGTTGGTGATCTTTG	ATGATGCCCAGGATAGCACTCACT
CRALBP	TTCCGCATGGTACCTGAAGAGGAA	ACTGCAGCCGGAAATTCACATAGC
GAPDH	CAACGGATTTGGTCGTATTGG	GCAACAATATCCACTTTACCACAGTTAA

892
893

bioRxiv preprint doi: https://doi.org/10.1101/796581; this version posted October 10, 2019. The copyright holder for this preprint (which was not certified by peer review) is the author/funder, who has granted bioRxiv a license to display the preprint in perpetuity. It is made available under aCC-BY-NC 4.0 International license.

894 **Table S3. List of GE vectors used.**
895

GE Vector Name	sgRNA Name	Vector Backbone	Backbone Source
LCv2.*AAVS1*	*AAVS1*	LentiCRISPRv2	Sanjana et al, Nat Methods, 2014
LCv2.R218C	R218C	LentiCRISPRv2	Sanjana et al, Nat Methods, 2014
LCv2.WT	WT	LentiCRISPRv2	Sanjana et al, Nat Methods. 2014
VMD2.*AAVS1*	*AAVS1*	*hVMD2-spCas9-T2A-GFP*	Alfred Lewin (University of Florida)
VMD2.R218C	R218C	*hVMD2-spCas9-T2A-GFP*	Alfred Lewin (University of Florida)
VMD2.WT	WT	*hVMD2-spCas9-T2A-GFP*	Alfred Lewin (University of Florida)
VMD2.N296H	N296H	*hVMD2-spCas9-T2A-GFP*	Alfred Lewin (University of Florida)
VMD2.A146K	A146K	*hVMD2-spCas9-T2A-GFP*	Alfred Lewin (University of Florida)

896
897

bioRxiv preprint doi: https://doi.org/10.1101/796581; this version posted October 10, 2019. The copyright holder for this preprint (which was not certified by peer review) is the author/funder, who has granted bioRxiv a license to display the preprint in perpetuity. It is made available under aCC-BY-NC 4.0 International license.

898 **Table S4. List of primers for lentiviral plasmid generation.**
899

Primer Name	Primer sequence
LCv2-GFP.Gib.F	GATTACAAAGACGATGACGATAAGGGATCCGGTGAGGGCAGAGGAAGTC
LCv2-GFP.Gib.	ACAGTCGAGGCTGATCAGCGGGTTTAAACCTACTACTGCTAGAGATTTTCCACAC
LCv2-GFP.seq.L	ACCGGCCTGTACGAGACACG
LCv2-GFP.seq.R	GAAAGGACAGTGGGAGTGGCACC
VMD2.LCv2.GFP.Gib.F	GTGGCACCGAGTCGGTGCTTTTTTGAATTCCAATTCTGTCATTTTACTAGGGTGATGAAATTC
VMD2.LCv2.GFP.Gib.R	TGTACTTCTTGTCCATGGTGGCAGCGCTCTATCGGCCGCGGGTACA
VMD2.LCv2.GFP.seq.L	GAATGAATACCGGGCTGCAGTCAAC
VMD2.LCv2.GFP.seq.R	GTCGGTGATCACGGCCCAG

900
901

bioRxiv preprint doi: https://doi.org/10.1101/796581; this version posted October 10, 2019. The copyright holder for this preprint (which was not certified by peer review) is the author/funder, who has granted bioRxiv a license to display the preprint in perpetuity. It is made available under aCC-BY-NC 4.0 International license.

Table S5. List of sgRNAs.

Off-target (Doench et al, Nat Biotechnol., 2016) and on-target (Hsu et al, Nat. Biotechnol., 2013) scores are also presented. Scores range from 0-100 with higher scores being better for both scoring systems. Highest ranked off-target cut sites for each sgRNA are available in **Supplemental Data File D**.

sgRNA Name	Sequence 5' - 3'	PAM	Chr	Position	Strand	Off-Target Score	On-Target Score
A146K	CTTTGGTGCTGACGCTGCGC	AGG	11	61955893	-1	81.2	51.6
R218C	GTGTCCACACTGAGTACACA	AGG	11	61957403	-1	56.3	67.2
WT	GTGTCCACACTGAGTACGCA	AGG	11	61957403	-1	86.5	63.7
N296H	CATCATCCTCTCCAAAGGGG	TGG	11	61959521	-1	54.0	64.6
AAVS1	GGGGCCACTAGGGACAGGAT	TGG	19	55115755	+1	55.8	54.5

bioRxiv preprint doi: https://doi.org/10.1101/796581; this version posted October 10, 2019. The copyright holder for this preprint (which was not certified by peer review) is the author/funder, who has granted bioRxiv a license to display the preprint in perpetuity. It is made available under aCC-BY-NC 4.0 International license.

910 **Table S6. Lentivirus titers.**
911

Lentivirus	Titer (Transduction units/ml)
hVMD2-hBEST1-T2A-GFP	$22x10^{6-7}$
LCv2.R218C sgRNA	$81.91\ x10^{6-7}$
LCv2.WT sgRNA	$55.22\ x10^{6-7}$
LCv2.*AAVS1* sgRNA	$45.43\ x10^{6-7}$
hVMD2-spCas9-T2A-GFP LV R218C sgRNA	$74.16\ x10^{6-7}$
hVMD2-spCas9-T2A-GFP LV WT sgRNA	$71.16\ x10^{6-7}$
hVMD2-spCas9-T2A-GFP LV A146K sgRNA	$74.26\ x10^{6-7}$
hVMD2-spCas9-T2A-GFP LV N296H sgRNA	$68.91\ x10^{6-7}$
hVMD2-spCas9-T2A-GFP LV *AAVS1* sgRNA	$74.01\ x10^{6-7}$

912
913

bioRxiv preprint doi: https://doi.org/10.1101/796581; this version posted October 10, 2019. The copyright holder for this preprint (which was not certified by peer review) is the author/funder, who has granted bioRxiv a license to display the preprint in perpetuity. It is made available under aCC-BY-NC 4.0 International license.

914 **Table S7. Primers for deep sequencing of DNA and cDNA.**
915

Primer Name	Primer sequence
MT.C.OT.5v2.HTS.F	GTTGGTTCCTGAAGATGGGCAG
MT.C.OT.5v2.HTS.R	CTGTCAAGGCCAAGTTCTGCTG
MT.C.OT.2.HTS.F	GCTAAATTCTGCTATAAAAGGAAGG
MT.C.OT.2.HTS.R	GCATTGCTTTAGAAAACTCAGAAGT
MT.C.OT.3.HTS.F	AGTGAGACCAAGTTCTGACAGCA
MT.C.OT.3.HTS.R	GGCCTCTTCATACATACACATGCAC
MT.C.OT.4.HTS.F	CCTCCACATCTGCAGAAAAGTGT
MT.C.OT.4.HTS.R	GGCAGGGTTTGGTCTCCTACTT
MT.C.OT.5.HTS.F	GGATGGCTCTGGGTGGGTTT
MT.C.OT.5.HTS.R	CTTCCAACTCTTCCTCCCACCC
MT.C.OT.6.HTS.F	TGAGGTTCAGAATAGCTCAGCA
MT.C.OT.6.HTS.R	TGTTTCTGTGAAGCAAATCAAAGCT
MT.C.OT.7.HTS.F	TGTTTCTGTGAAGCAAATCAAAGCT
MT.C.OT.7.HTS.R	TGAGGTTCAGAATAGCTCAGCA
MT.C.OT.8.HTS.F	AAAGCATGGCGGGAGTGCTAA
MT.C.OT.8.HTS.R	TGACTAAATCCCTGGCATCGCT
MT.C.OT.9.HTS.F	GCCAGTAATTTTCCAAGGCTTCT
MT.C.OT.9.HTS.R	TTCCTACTAGAACCTCCTTGAG
MT.C.OT.10.HTS.F	GTGACCTGACTTTGCTGAAAGGT
MT.C.OT.10.HTS.R	ACCTGAATTATCTCAAGCTCACT
AAVS1T2.HTS.F	ATGTGGCTCTGGTTCTGGGTAC
AAVS1T2.HTS.R	GAGACTAGGAAGGAGGAGGCCT
R218C.HTSv2.F	GTGTTCAGAACCCCATCCCC
R218C.HTSv2.R	AGCCTAGTCCTCACCTGTGT
BEST.cDNA.HTSv2.F	GGTCGAATCCGGGACCCTATC
BEST.cDNA.HTSv2.R	GCCACAGTCACCACCTGTGTAT
AAVS1T2.HTS.F	ATGTGGCTCTGGTTCTGGGTAC
AAVS1T2.HTS.R	GAGACTAGGAAGGAGGAGGCCT

916
917

bioRxiv preprint doi: https://doi.org/10.1101/796581; this version posted October 10, 2019. The copyright holder for this preprint (which was not certified by peer review) is the author/funder, who has granted bioRxiv a license to display the preprint in perpetuity. It is made available under aCC-BY-NC 4.0 International license.

Table S8. Number of cells used for CaCC current density measurements.

Line	Replicate #1		Replicate #2		Total	
	0 calcium	4.5 µM calcium	0 calcium	4.5 µM calcium	0 calcium	4.5 µM calcium
Control	3	3	5	3	8	6
Isogenic control	5	7	4	3	9	10
R141H/A195V*	4	3	4	5	12*	12*
R141H/A195V +GA	2	3	3	4	5	7
R218C	3	3	5	2	8	5
R218C +GA	6	7	3	4	9	11
R218C +GE (R218C sgRNA)	3	5	4	5	7	10
N296H	4	4	4	3	8	7
N296H +GA	4	3	2	4	6	7
N296H +GE (N296H sgRNA)	4	5	5	4	9	9
A146K	2	2	5	3	7	5
A146K +GA	4	2	4	3	8	5
A146K +GE (A146K sgRNA)	5	5	5	6	10	11
A146K +GE (*AAVS1* sgRNA)	4	3	5	3	9	6

*3 replicates were used for R141H/A195V. Replicate #3 for R141H/A195V had n=4 (0 calcium); n=4 (4.5 µM calcium)

References for Supplemental Tables

Doench, J.G., Fusi, N., Sullender, M., Hedge, M., Vaimberg, E.W., Donovan, K.F., Smith, I., Tothova, Z., Wilen C., Orchard, R., Virgin, H.W., Listgarten, J., and Root, D.E. (2016). Optimized sgRNA design to maximize activity and minimize off-target effects of CRISPR-Cas9. Nat Biotechnol *34(2)*, 184-191.

Hsu, P.D., Scott, D.A., Weinstein, J.A., Ran, F.A., Konermann, S., Agarwala, V., Li, Y., Fine, E.J., Wu, X., Shalem, O., Cradick, T.J., Marraffini, L.A., Bao, G., and Zhang, F. (2013). DNA targeting specificity of RNA-guided Cas9 nucleases. Nat Biotech *31*, 827-832.

bioRxiv preprint doi: https://doi.org/10.1101/796581; this version posted October 10, 2019. The copyright holder for this preprint (which was not certified by peer review) is the author/funder, who has granted bioRxiv a license to display the preprint in perpetuity. It is made available under aCC-BY-NC 4.0 International license.

933 Sanjana, N., Shalem, O., and Zhang, F. (2014). Improved vectors and genome-wide libraries for CRISPR
934 screening. Nat Methods *11,* 783-784.
935
936 Singh, R., Shen, W., Kuai, D., Martin, J.M., Guo, X.R., Smith, M.A., Perez, E.T., Phillips, M.J., Simonett, J.M.,
937 Wallace, K.A.*, et al.* (2013b). iPS cell modeling of Best disease: insights into the pathophysiology of an inheritec
938 macular degeneration. Hum Mol Genet *22*, 593-607.
939
940 Steyer, B., Bu, Q., Cory, E., Jiang, K., Duong, S., Sinha, D., Steltzer, S., Gamm, D., Chang, Q., and Saha,
941 K. (2018). Scarless Genome Editing of Human Pluripotent Stem Cells via Transient Puromycin Selection.
942 Stem Cell Reports *10*, 642-654.